PHYSICAL REVIEW FLUIDS **11**, 054101 (2026)

Newtonian die-swell phenomenon revisited: Theory and simulations

W.-P. Breugem * and Y. E. Kamis
Laboratory for Aero & Hydrodynamics, Process & Energy Department, Delft University of Technology, Mekelweg 2, 2628 CD Delft, The Netherlands

(Received 22 January 2026; accepted 17 April 2026; published 6 May 2026)

The laminar jet of a Newtonian liquid emanating from a long circular nozzle into a gaseous environment is studied. Provided that gravity effects can be neglected, the flow depends solely on the Reynolds number (Re) and the Capillary number (Ca) based on the nozzle bulk velocity (U_b). At high Re, the jet contracts downstream of the nozzle, while at low Re, the jet expands, which is known as the Newtonian die-swell phenomenon. To study the influence of Re on the jet behavior, an integral momentum balance is theoretically derived for the entire flow, both in the nozzle and in the jet. A useful decomposition is made of the viscous force in the integral momentum balance into a contribution from the excess wall pressure drop (P_{exc}) and a contribution from the excess integral wall shear stress (T_{exc}) relative to, respectively, the pressure drop and integral wall shear stress for Poiseuille flow. The results of the numerical simulations for $\text{Re} \in [4.2 : 47.4]$ show that P_{exc} is larger than zero for $\text{Re} \lesssim 6$, while negative for $\text{Re} \gtrsim 6$. Furthermore, T_{exc} is always negative and is the dominant contribution to the overall viscous force for $\text{Re} \lesssim 12$. Normalized by the integral wall shear stress for Poiseuille flow, T_{exc} appears to scale with $\text{Re}^{-1/3}$, implying that axial velocity perturbations near the nozzle wall scale with $\text{Re}^{-1/3}$ too when normalized by U_b. Self-similar behavior is also found for the axial velocity perturbation at the nozzle centerline, which scales with $\text{Re}^{-2/3}$ when normalized by U_b. The observed power-law scalings in Re are explained theoretically from the development of a boundary layer along the jet interface, originating from the stick-slip transition at the nozzle lip, and the constant integral mass flux along the jet. The boundary-layer flow is responsible for axial viscous stresses at the nozzle exit plane that result in a perturbation flow within the nozzle over an axial distance on the order of the nozzle radius. The die-swell phenomenon at low Re is caused by the radially outward flow at the nozzle exit and the accompanying compressive normal viscous stress that pushes the interface outwards till equilibrium is achieved. Self-similar behavior is also found for the perturbation flow far downstream of the nozzle with respect to the plug flow at equilibrium. With increasing Re, the exponential decay rate of the perturbation in the centerline velocity converges toward a prediction first made by Bohr for a related problem [N. Bohr, Philos. Trans. R. Soc. A **209**, 281 (1909)], while the exponential decay rate of the perturbation in the jet radius is approximately twice as high. Finally, a discussion is given of the implications of our findings for applications in practice.

DOI: 10.1103/l1b2-blw2

*Contact author: w.p.breugem@tudelft.nl

I. INTRODUCTION

The die-swell phenomenon refers to the swelling of a viscoelastic liquid jet when the liquid is forced through a long die or nozzle [1]. It is generally believed that the increase in the jet diameter originates from the elastic relaxation of the viscoelastic liquid (typically a polymer) due to the transition from a stick to a slip boundary condition for the flow at the exit of the nozzle. In literature, several correlations have been proposed in which the increase in the jet diameter is correlated with the first normal stress difference at the nozzle wall [2,3]. Less well known is that die swell may also occur for purely Newtonian liquids, which is sometimes referred to as the *Newtonian die-swell phenomenon*. This was first observed in experiments by Middleman and Gavis [4] on Newtonian liquid jets at Reynolds numbers below $\mathrm{Re} = \rho U_b 2R/\eta \lesssim 14$, where ρ is the fluid density, η is the fluid viscosity, U_b is the bulk velocity within the nozzle and R is the radius of the circular nozzle. The swelling increased for lower Re and amounted more than 10% of the nozzle radius at $\mathrm{Re} \approx 2$, the lowest investigated Reynolds number. For $\mathrm{Re} \gtrsim 14$, the jet contracted toward an equilibrium radius, R_∞, smaller than the nozzle radius; see the sketch in Fig. 1. The jet expansion or contraction ratio, $\chi = R_\infty/R$, monotonically decreased with Re and approached the theoretical limit of $\chi = \sqrt{3}/2$ for $\mathrm{Re} \gtrsim 150$. This limit was first derived by Harmon [5], based on assuming (a) Poiseuille flow at the exit of a long circular nozzle, (b) plug flow in the jet far downstream of the nozzle, and (c) conservation of the integral mass and the integral momentum flux along the jet.

Experiments by Batchelor *et al.* [6] provided further evidence of the Newtonian die-swell phenomenon at $\mathrm{Re} \approx 10^{-8}$, showing an increase of approximately 13.5% in the jet radius for a highly viscous Newtonian fluid. Obviously, the Newtonian die-swell phenomenon cannot be explained from an elastic relaxation effect. Over the years, different mechanisms were proposed to explain this phenomenon. Middleman and Gavis [4] attributed the jet expansion to a relaxation effect of the axial viscous stress downstream of the nozzle exit and, more specifically, to a nonzero, positive value for the integral of the axial viscous stress over the nozzle exit plane. Gavis and Modan [7] pointed out that this integral is actually zero for a Newtonian fluid, since the integral mass flux is constant everywhere in the flow. Instead, they suggested that the expansion originates from a pressure decrement at the nozzle exit that acts as a tensile stress on the flow. In contrast with this, Nickell *et al.* [8] suggested that the presence of a compressive stress at the center of the nozzle exit is likely the main cause of the jet expansion. More recently, Haustein *et al.* [9] argued that the loss of kinetic energy through viscous dissipation must be compensated by an expansion of the jet to maintain a constant integral mass flux.

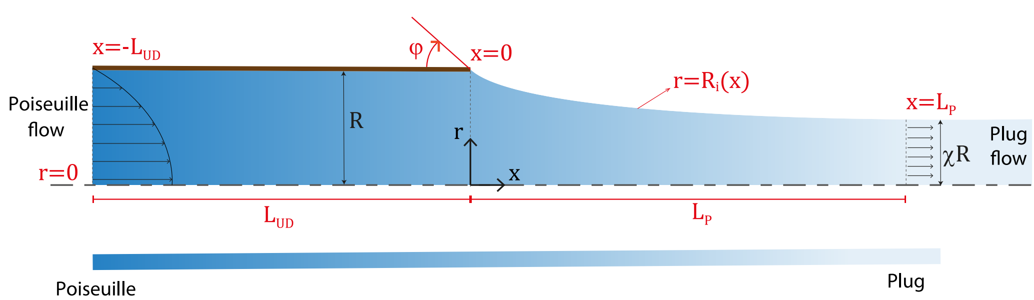

FIG. 1. Sketch of the flow geometry considered in the present study. L_{UD} is the distance upstream of the nozzle exit plane over which the flow deviates from homogeneous Poiseuille flow. L_P is the distance downstream of the nozzle exit plane over which the flow deviates from uniform plug flow. The jet contraction ratio, χ, is defined as the ratio of the jet radius in the plug flow region to the nozzle radius R. φ is the angle of the jet interface with respect to the nozzle wall at the nozzle exit. $R_i(x)$ is the local radius of the jet as function of the downstream distance, x, from the nozzle exit plane.

For Newtonian liquid jets issued from capillary needles, Goren and Wronski [10] studied the transition from an expanding jet to a contracting jet when Re is gradually increased. Interestingly, for $12 \lesssim \mathrm{Re} \lesssim 17$, their experiments revealed a nonmonotonic behavior of the jet radius as function of the streamwise distance from the nozzle exit, where the initial contraction is followed by an expansion toward the final equilibrium radius further downstream. For $\mathrm{Re} \lesssim 14$, the equilibrium radius was smaller than the nozzle radius, and the opposite was true for $\mathrm{Re} \gtrsim 14$, in agreement with the findings of Middleman and Gavis [4].

Further experiments were reported by Gear *et al.* [11]. Measured jet velocity profiles were in reasonably good agreement with Goren and Wronski [10], provided that the normalized axial distance of the jet profiles of Goren and Wronski was multiplied by a factor two; this was attributed to a typo in the axis label of Fig. 2 in Goren and Wronski [10]. Gear *et al.* [11] also reported measurements of the pressure distribution along the centerline and of the axial velocity profile at the exit plane of the nozzle. No details were provided on the measurement techniques used. At $\mathrm{Re} = 100$, a clear minimum in the centerline pressure profile was found slightly downstream of the nozzle exit, which was lower than the ambient pressure. At $\mathrm{Re} = 0.05$, the centerline velocity at the exit of the nozzle was significantly reduced compared to the expected value for fully developed Poiseuille flow, while the opposite was true for the velocity near the edge of the nozzle. In contrast, at $\mathrm{Re} = 100$, the velocity profile at the exit of the nozzle was close to the fully developed profile.

By linearizing the Navier-Stokes equations around the final equilibrium state of the jet downstream of the nozzle, Goren and Wronski [10] showed theoretically that the perturbations in the jet radius and the jet velocity field with respect to the equilibrium state should decay exponentially in x/R_∞, the distance normalized by the equilibrium jet radius. For $\mathrm{Re}_\infty = \mathrm{Re}/\chi \gtrsim 40$, the predicted exponential decay rate is approximately equal to $29.36/\mathrm{Re}_\infty$, a theoretical result first derived by Bohr [12] for a related flow problem. However, Goren and Wronski [10] reported that the measured exponential decay rate of the jet radius was about twice as large as expected at high Re_∞, which was attributed to nonnegligible higher-order terms in the series solution for the perturbation stream function [10].

In a related study, Goren [13] theoretically analyzed the jet behavior near the nozzle exit. He argued that a boundary layer develops along the jet interface in which the shear flow adjusts itself to the free-slip condition at the interface. Considering a two-dimensional boundary-layer flow under uniform shear, assuming a sufficiently high Reynolds number and ignoring the interaction of the boundary-layer flow with the shear flow in the jet core, it was found that a self-similar solution exists for the boundary-layer flow. The contraction of the jet radius and the jet surface velocity were predicted to scale both with $x^{1/3}$. The experiments of Goren and Wronski [10] confirmed this scaling for the jet radius near the nozzle exit, albeit with a significantly lower prefactor than predicted by the boundary-layer theory.

Tillett [14] extended the analysis of Goren for a two-dimensional jet by including the interaction of the boundary-layer flow with the flow in the jet core as well as the interaction of the jet flow with the flow inside the nozzle. Using the method of matched asymptotic expansions, he recovered Goren's results for the jet contraction and jet surface velocity near the nozzle exit as the leading-order term of the expansions for high Re.

Duda and Vrentas [15] performed another theoretical analysis, but for jets issued from a circular nozzle. Instead of using cylindrical coordinates, they adopted a Protean coordinate system in which the radial coordinate was replaced by the Stokes stream function with the obvious advantage that the jet surface corresponds to a constant value of the stream function. Assuming a sufficiently high Reynolds number, an approximate equation was derived for the boundary-layer flow in the Protean coordinate system. Numerical solutions of this equation for horizontal jets with a prescribed Poiseuille velocity profile at nozzle exit, indicated a much faster convergence for the jet radius toward equilibrium than for the axial velocity.

Duda and Vrentas [15] also derived an approximate solution for the jet flow field by linearizing their boundary-layer equation around a reference state with a uniform velocity equal to the nozzle bulk velocity. Though this is a questionable approach, as they already mentioned themselves, the approximate solution was found to be in a good agreement with the numerical solution of the nonlinear boundary-layer equation for a vertical jet. For horizontal jets, they found an exponential decay of the jet velocity toward equilibrium in the far field. Interestingly, the decay rate of the leading-order term in their series solution is equal to Bohr's prediction for a high Reynolds number, but based on Re instead of Re_∞ and for an exponential decay in x/R instead of x/R_∞. The limiting jet behavior is thus inconsistent with the theoretical analysis of Goren and Wronski [10]. In this respect, it should be noted that Goren and Wronski [10] linearized the full Navier-Stokes equations around the equilibrium state of the jet in the far field, while Duda and Vrentas [15] linearized their boundary-layer equation around a fictitious state with a different velocity.

For the high Reynolds number regime, Philippe and Dumargue [16] derived theoretical approximations for a contracting liquid jet from a vertical circular nozzle using the method of matched asymptotic expansions. Surface tension was neglected, but gravity was included in their analysis. Furthermore, Poiseuille flow was assumed at the nozzle exit, thus excluding any interaction of the jet with the upstream flow within the nozzle. Goren's boundary-layer results for the scaling of the jet contraction and jet surface velocity were recovered as the leading-order term of the respective expansions for the boundary-layer region. The asymptotic expansions for the flow field near the nozzle and further away from the nozzle, were in good agreement with holography-based optical measurements of the velocity field [17] for $\rho g R/(\eta U_b/R)$ in the range of 11 till 47 with g the gravitational acceleration magnitude (thus corresponding to a regime in which the effect of gravity on the jet flow was relatively strong).

For the Stokes regime ($\mathrm{Re} = 0$), Trogdon and Joseph theoretically analyzed the expansion of the jet at high [18] and small surface tension [19]. Assuming that the expansion of the jet is small, the boundary conditions at the jet's free surface were linearized. The linearized problem was solved by matching the eigenfunction expansions for the Stokes stream function for the nozzle and the jet region at the nozzle exit. For high surface tension, the jet expansion ratio was found to scale linearly with the Capillary number, $\mathrm{Ca} = \eta U_b/\gamma$, where γ the surface tension coefficient. In the limit of zero surface tension, $\mathrm{Ca} \to \infty$, the jet expansion ratio approached a value of $\chi = 1.111$. Although close, this is somewhat below the limiting value found in the experiments of Batchelor *et al.* [6] ($\chi \approx 1.135$) and the values obtained from finite-element simulations by Mitsoulis *et al.* [20] ($\chi = 1.127$) and Georgiou and Boudouvis [21] ($\chi = 1.1265$, using singular basis functions to capture the stress singularity at the nozzle lip). This discrepancy is likely related to the linearization applied by Trogdon and Joseph.

As mentioned earlier, to obtain the theoretical limit of the jet contraction ratio of $\chi = \sqrt{3}/2$ at high Re, Harmon [5] assumed that the integral momentum flux is conserved along the jet, thus neglecting any forces acting on the flow. Naturally, his work was later extended by others by including effects of gravity, surface tension and viscosity into a formulation of the integral momentum balance for the jet. Joseph [22] provides a literature review of several attempts made to derive the full integral momentum balance, and discusses fundamental flaws in many of these attempts related to, for example, an incorrect treatment of surface tension or an incorrect assumption of Poiseuille flow at the nozzle exit. Since at finite Re the flow at the nozzle exit will deviate from Poiseuille flow, Joseph [22] derived an integral momentum balance for the entire flow within both the nozzle and the jet, extending from Poiseuille flow sufficiently far upstream of the nozzle exit till plug flow sufficiently far downstream of the nozzle exit. He argued that viscous effects are responsible for an excess of the skin friction within the nozzle compared to Poiseuille flow and thus for a reduction of the integral momentum flux. Furthermore, he assumed that the excess skin friction scales with Re^n when normalized by the skin friction for Poiseuille flow. By neglecting surface tension and gravity, the integral momentum balance reduced to a quadratic equation for the jet contraction ratio. The power exponent in the expression for the excess skin friction was estimated by fitting the solution of this quadratic equation to experimental data from literature, from which it was found that $n \approx 1/3$ for $\mathrm{Re} \gtrsim 10$.

Over the past 50 years, several numerical studies have been performed on liquid jets issued from circular nozzles. In all cases discussed below, the finite-element method was used. Nickell *et al.* [8] were one of the first to conduct simulations of the Newtonian die-swell phenomenon for a horizontal jet. Surface tension was not included. Good agreement was found for the jet shape and expansion ratio with experiments of Batchelor *et al.* [6]. Omodei [23] performed simulations of horizontal liquid jets for Reynolds number ranging from 10^{-4} till 10^3 and also studied the influence of surface tension. Good agreement was found with experimental data of Goren and Wronski [10] for expanding and contracting liquid jets. Georgiou *et al.* [24] extended the work of Omodei [23] by considering a larger span in Reynolds numbers and surface tension values. At Re $= 4000$, the jet contraction ratio was 0.867, thus very close to the theoretical estimate of Harmon [5]. Surface tension was shown to counteract the deviation of the jet radius from the nozzle radius. Mitsoulis *et al.* [20] performed a comprehensive parameter study of factors affecting the jet shape, which also included effects such as compressibility, pressure-dependence of the viscosity and slip at the nozzle wall. More recently, Haustein *et al.* [9] performed simulations of both horizontal and vertical liquid jets and developed empirical models to predict the jet contraction ratio as function of the relevant parameters.

The aim of the present study is to unravel the influence of the Reynolds number on the behavior of laminar liquid jets issued from a long circular nozzle, with a particular focus on the transition from expanding to contracting jets when the Reynolds number is gradually increased. The influence of gravity is assumed to be negligible. The main research questions are: (1) What are the correct expressions of the surface tension and viscous forces in the integral momentum balance for the flow in the nozzle and the jet? (2) What is the physical mechanism underlying the expansion of liquid jets at low Reynolds number? (3) What evidence can be found of self-similar behavior of the flow within the jet and inside the nozzle? (4) What can be deduced about the Re-scaling of the viscous force in the integral momentum balance from the observed self-similar behavior of the flow? To address these questions, the integral momentum balance of the jet is derived theoretically from first principles and analyzed for the limiting jet behavior in specific flow regimes. To assess the self-similar behavior of the flow and the viscous contribution to the integral momentum balance, numerical simulations have been performed of expanding and contracting laminar jets issued from a long circular nozzle for Re $\in [4.2 : 47.4]$ using the computational fluid dynamics (CFD) finite-volume solver OpenFOAM [25].

The remainder of this manuscript is structured as follows. In Sec. II, a detailed derivation is given for the integral momentum balance. In Sec. III, the numerical method and computational setup are explained. In Sec. IV, the results from the numerical simulations are analyzed. Finally, in Sec. V, the main conclusions are summarized, followed by a discussion of perspectives for future research and implications of our findings for applications in practice.

II. INTEGRAL MOMENTUM BALANCE

A. Derivation

Following Joseph [22], we consider the entire flow, which extends from fully developed Poiseuille flow at $x = -L_{\mathrm{UD}}$ inside the nozzle till fully developed plug flow at $x = L_p$ downstream of the nozzle; see the sketch of the considered flow geometry in Fig. 1. We will first derive the integral momentum balance for the flow inside the nozzle, then for the flow outside the nozzle, after which the two balance equations are added together to obtain the overall integral momentum balance for the entire flow.

To begin with, the set of equations for an incompressible liquid flow in steady state is given by

$$\nabla \cdot \mathbf{u} = 0, \tag{1a}$$

$$\rho \nabla \cdot \mathbf{u}\mathbf{u} = -\nabla p + \nabla \cdot \boldsymbol{\tau} + \rho \mathbf{g}, \tag{1b}$$

where $\mathbf{u}$ is the velocity vector, p is the pressure, $\boldsymbol{\tau} = \eta[\nabla\mathbf{u} + \nabla\mathbf{u}^T]$ is the viscous stress tensor for a Newtonian fluid, $\mathbf{g}$ is the gravitational acceleration vector and assumed to act in the direction of the main flow, ρ is the mass density, and η is the dynamic viscosity of the liquid. The density and the viscosity of the gaseous environment outside the jet are assumed to be very small. Consequently, the ambient pressure is approximately uniform and any influence of the ambient flow on the jet dynamics can be safely neglected. Moreover, as mentioned in the introduction, we will assume in the following that the influence of gravity is negligible; later on, we will assess the conditions under which this assumption is valid.

For $x \leqslant -L_{\mathrm{UD}}$, the steady unidirectional Poiseuille flow exhibits a parabolic velocity profile given by

$$u(r) = -\frac{dp}{dx}\frac{R^2}{4\eta}\left(1 - \frac{r^2}{R^2}\right), \tag{2}$$

where dp/dx is the streamwise pressure gradient that drives the flow, R is the nozzle radius, and r is the radial distance measured from the nozzle centerline. The bulk velocity within the nozzle, U_b, is obtained by integrating the velocity profile over the radius:

$$U_b = -\frac{dp}{dx}\frac{R^2}{8\eta}. \tag{3}$$

The integral mass and momentum fluxes across the plane $x = -L_{\mathrm{UD}}$ are given by, respectively:

$$\dot{m}_{\mathrm{UD}} = \int_0^R \rho u(r) 2\pi r dr = \rho\pi R^2 U_b, \tag{4a}$$

$$\dot{M}_{\mathrm{UD}} = \int_0^R \rho u(r)^2 2\pi r dr = \tfrac{4}{3}\rho\pi R^2 U_b^2. \tag{4b}$$

For $x \geqslant L_P$, the flow is assumed to be plug flow with a uniform velocity, U_∞, and a constant jet radius, R_∞, provided that the stretching due to gravity is negligible. The mass and momentum fluxes through the plane at $x = L_P$ are given by, respectively:

$$\dot{m}_p = \int_0^{R_\infty} \rho U_\infty 2\pi r dr = \rho\pi(\chi R)^2 U_\infty, \tag{5a}$$

$$\dot{M}_p = \int_0^{R_\infty} \rho U_\infty^2 2\pi r dr = \rho\pi(\chi R)^2 U_\infty^2, \tag{5b}$$

where $\chi = R_\infty/R$ is the jet contraction ratio.

Mass conservation dictates that the mass fluxes given by Eqs. (4a) and (5a) must be equal to each other, yielding $U_b = \chi^2 U_\infty$. Likewise, in the *inertial regime* (i.e., when gravity, viscous and capillary forces are negligible), the momentum fluxes given by Eqs. (4b) and (5b) must be equal, which implies that $\chi = \sqrt{3}/2 \approx 0.866$ and thus a contraction of the jet by approximately 13.4%, a theoretical result that was first reported by Harmon [5].

Between $x = -L_{\mathrm{UD}}$ and $x = L_P$, the flow is altered by a combination of inertia, gravity, viscous stresses, and surface tension. The integral momentum balance for the region upstream of the nozzle exit plane is obtained from integrating Eq. (1b) over the region $x \in [-L_{\mathrm{UD}}, 0]$:

$$\dot{M}_0 - \dot{M}_{\mathrm{UD}} = -\int_0^R (p|_{x=0} - p|_{x=-L_{\mathrm{UD}}}) 2\pi r dr + \int_{-L_{\mathrm{UD}}}^0 \tau_{xr}|_{r=R}\, 2\pi R dx, \tag{6}$$

where the effect of gravity is neglected, $\dot{M}_0$ is the integral momentum flux at the nozzle exit, and we used that for a Newtonian fluid $\int_0^R \tau_{xx} 2\pi r dr = 2\eta \frac{\partial}{\partial x}(\int_0^R u 2\pi r dr) = 0$ inside the nozzle since $u(0, R) = 0$ and $\int_0^R u 2\pi r dr = \pi R^2 U_b$ is constant in x.

Beyond the nozzle exit at $x = 0$, one has the stress boundary conditions at the free surface denoted by $r = R_i(x)$:

$$p(x, R_i(x)) = p_{\text{atm}} + \gamma\kappa + (\mathbf{n} \cdot \boldsymbol{\tau} \cdot \mathbf{n})_i, \tag{7a}$$

$$(\mathbf{t} \cdot \boldsymbol{\tau} \cdot \mathbf{n})_i = 0, \tag{7b}$$

where p_{atm} is the atmospheric pressure outside the jet, γ is the surface tension coefficient, κ is the local interface curvature, $\mathbf{n}$ is the outward unit normal vector at the interface, and $\mathbf{t}$ is the unit tangent vector along the interface. In cylindrical coordinates (r, θ, x), the latter two vectors can be expressed as function of the jet radius by, respectively:

$$\mathbf{n} = \frac{1}{\left(1 + R_i'^2\right)^{1/2}} \begin{bmatrix} 1 \\ 0 \\ -R_i' \end{bmatrix}, \qquad \mathbf{t} = \frac{1}{\left(1 + R_i'^2\right)^{1/2}} \begin{bmatrix} R_i' \\ 0 \\ 1 \end{bmatrix}, \tag{8}$$

where the prime denotes differentiation with respect to x, thus $R_i' = dR_i/dx$. Similarly, the surface curvature can be expressed as function of the jet radius according to

$$\kappa = \frac{1}{R_i R_i'} \frac{d}{dx} \left(\frac{R_i}{\sqrt{1 + R_i'^2}} \right). \tag{9}$$

The integral momentum balance for the region downstream of the nozzle can be obtained by integrating Eq. (1b) over the region $x \in [0, L_P]$. Using the normal stress condition on the jet interface given by Eq. (7a), the following result is obtained:

$$\begin{aligned} \dot{M}_P - \dot{M}_0 = \int_0^R p\, 2\pi r dr|_{x=0} - \underbrace{\int_0^{\chi R} p\, 2\pi r dr|_{x=L_P}}_{F_1} + \underbrace{\int_0^{L_P} p_{\text{atm}}\, R_i' 2\pi R_i dx}_{F_2} + \underbrace{\int_0^{L_P} \gamma\kappa\, R_i' 2\pi R_i dx}_{F_3} \\ + \underbrace{\int_0^{L_P} (\mathbf{n} \cdot \boldsymbol{\tau} \cdot \mathbf{n})_i\, R_i' 2\pi R_i dx}_{F_4} + \underbrace{\int_0^{L_P} [-(\tau_{xx})_i \cdot R_i' + (\tau_{xr})_i] 2\pi R_i dx}_{F_5}, \end{aligned} \tag{10}$$

where the effect of gravity is neglected as before. Note that we used again that $\int_0^R \tau_{xx}|_{x=0} 2\pi r dr = 0$ for a Newtonian fluid. Thus, the *direct* contribution from axial viscous stresses to the integral momentum balance of the jet is equal to zero, contrary to a number of previous studies that attribute viscous effects on the jet contraction ratio to this term [4,26,27].

At finite Reynolds numbers, $\dot{M}_0 \neq \dot{M}_{\text{UD}}$, even in the absence of gravity, contrary to what has been often assumed in literature [4,15,26–28]. This can be related to viscous effects within the nozzle; see Eq. (6). This *indirect* effect constitutes the viscous contribution to the jet contraction ratio.

Using that at $x = L_p$ the pressure is equal to $p = p_{\text{atm}} + \gamma/(\chi R)$, the pressure force F_1 in Eq. (10) can be rewritten as

$$F_1 = p_{\text{atm}} \pi \chi^2 R^2 + \pi \chi R \gamma. \tag{11a}$$

The force F_2 exerted by the atmospheric pressure on the jet interface is equal to

$$F_2 = p_{\text{atm}} \pi R^2 (\chi^2 - 1). \tag{11b}$$

Using Eq. (9), the capillary force F_3 can be worked out into the following expression:

$$F_3 = 2\pi R \gamma [\chi - \cos\varphi], \tag{11c}$$

where φ is the angle of the interface with respect to the nozzle wall at the nozzle exit; see Fig. 1. To determine the viscous forces F_4 and F_5 exerted by the free surface on the jet flow, one needs to evaluate the stress conditions at the interface, Eqs. (7a) and (7b), by using Eq. (8):

$$(\mathbf{n}\cdot\boldsymbol{\tau}\cdot\mathbf{n})_i = \frac{(\tau_{rr})_i - (\tau_{xx})_i R_i'^2}{1 - R_i'^2}, \tag{12a}$$

$$(\mathbf{t}\cdot\boldsymbol{\tau}\cdot\mathbf{n})_i = \frac{R_i'(\tau_{rr})_i + \left(1 - R_i'^2\right)(\tau_{xr})_i - R_i'(\tau_{xx})_i}{1 + R_i'^2} = 0. \tag{12b}$$

Solving Eq. (12b) for the shear component at the interface, $(\tau_{xr})_i$, yields

$$(\tau_{xr})_i = [(\tau_{xx})_i - (\tau_{rr})_i]\frac{R_i'}{1 - R_i'^2}. \tag{13}$$

Substituting Eq. (12a) into the expression for F_4 and Eq. (13) into the expression for F_5 in Eq. (10), reveals that $F_4 = -F_5$ and thus that the sum of the viscous forces exerted by the jet interface is zero, as may already be intuitively expected.

The overall integral momentum balance for the flow in both the nozzle and the jet is given by the summation of Eqs. (6) and (10):

$$\begin{aligned}\dot{M}_P - \dot{M}_{\mathrm{UD}} = \underbrace{[p|_{x=-L_{\mathrm{UD}}} - (p_{\mathrm{atm}} + \gamma\kappa_0)]\pi R^2 + \int_{-L_{\mathrm{UD}}}^{0} \tau_{xr}|_{r=R} 2\pi R dx}_{F_{\mathrm{visc}}} \\ + \underbrace{\gamma\pi R[\chi - \cos\varphi - RR_i''(0)\cos^3\varphi]}_{F_{\mathrm{cap}}},\end{aligned} \tag{14}$$

where $\kappa_0 = \cos\varphi/R - R_i''(0)\cos^3\varphi$ is the interface curvature at the nozzle exit using that $\cos\varphi = 1/\sqrt{1 + R_i'^2}$ at $x = 0$. The forces on the right-hand side represent, respectively, the net viscous force and the net capillary force acting on the flow.

Note that in deriving Eq. (14), we subtracted a term $\gamma\kappa_0\pi R^2$ from the first term on the right-hand side and added the same term to the second term on the right-hand side. This was done since the last term on the right-hand side now represents the complete capillary force acting on the flow from the line tension force at the nozzle exit ($F_{\mathrm{cap},1} = -2\pi\gamma R\cos\varphi$), the line tension force at $x = L_P$ ($F_{\mathrm{cap},2} = 2\pi\gamma\chi R$), the Laplace pressure acting on the nozzle exit plane ($F_{\mathrm{cap},3} = \gamma\pi R[\cos\varphi - R_i''(0)R\cos^3\varphi]$), and the Laplace pressure acting on the plane at $x = L_P$ ($F_{\mathrm{cap},4} = -\gamma\pi\chi R$). The sum of the four contributions is equal to the total capillary force, $F_{\mathrm{cap}} = \sum_{i=1}^{4} F_{\mathrm{cap},i}$. Furthermore, note that in the expression of the viscous force, $p|_{x=-L_{\mathrm{UD}}} - (p_{\mathrm{atm}} + \gamma\kappa_0) = p|_{x=-L_{\mathrm{UD}}} - (p - \mathbf{n}\cdot\boldsymbol{\tau}\cdot\mathbf{n})_{0,R}$ based on Eq. (7a). This is equal to the wall pressure difference over the nozzle, Δp_w, but excluding the contribution from the stress singularity at the nozzle lip [22,29].

Equation (14) is essentially the same as derived before by Joseph [22] albeit in a different form. However, Joseph subtracted and added a term $\gamma\pi R$ instead of $\gamma\kappa_0\pi R^2$ to the right-hand side of the integral momentum balance, suggesting a net capillary force equal to $\gamma\pi R[\chi + R - 2\cos\varphi]$. This is not equal to the net capillary force derived above. The difference between the two expressions is equal to $\gamma\pi R[1 - \cos\varphi + RR_i''(0)\cos^3\varphi]$. Taking into account that φ is small and therefore that $\cos\phi \approx 1$, the difference is approximately equal to $\gamma\pi R \cdot RR_i''(0)$. The nondimensional curvature $RR_i''(0)$ depends on the flow parameters, but for the highly viscous regime an estimate can be made based on the parametrization of the jet profile given by Batchelor *et al.* [6]: $RR_i''(0) \approx -0.57$. Finally, we remark that both our expression for the net capillary force and the expression derived by Joseph [22] satisfy the expected limit of $F_{\mathrm{cap}}/\gamma \to 0$ for $\gamma \to \infty$, when $\chi = 1$ and the jet is a straight cylinder with a uniform radius equal to R. This limiting behavior will be discussed in more detail later.

Since we have identified the second term on the right-hand side of Eq. (14) as the overall capillary force, we find that the first term on the right-hand side must represent the overall viscous force contribution to the integral momentum balance. Again, our expression for the viscous force is different from the expression derived by Joseph [22], originating from his approximation of the interface curvature at the nozzle exit by $1/R$. When surface tension is negligible, his and our expression for the viscous force are essentially the same, albeit expressed in a different form.

Equation (14) is made nondimensional using the nozzle radius R as a characteristic length scale, U_b as a characteristic velocity scale and $\eta U_b/R$ as a characteristic scale for the viscous shear stress and pressure variations. By substituting the expressions for the integral momentum fluxes given by Eqs. (4b) and (5b) into Eq. (14), dividing the result by $\rho\pi R^2 U_b^2$ and after normalization with the above scales, we obtain

$$\frac{1}{\chi^2} - \frac{4}{3} = \frac{1}{\mathrm{Re}}\tilde{K} + \frac{1}{\mathrm{We}}[\chi - \cos\varphi - \tilde{R}_i''(0)\cos^3\varphi], \tag{15}$$

where the tilde denotes normalization by the appropriate scale, $\mathrm{Re} = \rho U_b 2R/\eta$ is the Reynolds number and $\mathrm{We} = \rho U_b^2 R/\gamma$ is the Weber number. The first term on the right-hand side is the nondimensional viscous force, with $\tilde{K}$ defined according to

$$\tilde{K} = \tilde{P}_{\mathrm{exc}} + \tilde{T}_{\mathrm{exc}}, \tag{16a}$$

$$\tilde{P}_{\mathrm{exc}} = 2\left[\tilde{p}|_{\tilde{x}=-\tilde{L}_{\mathrm{UD}}} - \left(\tilde{p}_{\mathrm{atm}} + \frac{\tilde{\kappa}_0}{\mathrm{Ca}}\right) - \Delta\tilde{p}^H\right], \tag{16b}$$

$$\tilde{T}_{\mathrm{exc}} = 4\int_{-\tilde{L}_{\mathrm{UD}}}^{0} \left(\tilde{\tau}_{xr}|_{\tilde{r}=1} - \tilde{\tau}_{xr}^H|_{\tilde{r}=1}\right) d\tilde{x}, \tag{16c}$$

where we refer to $\tilde{P}_{\mathrm{exc}}$ as the nondimensional *excess wall pressure drop* and to $\tilde{T}_{\mathrm{exc}}$ as the nondimensional *excess integral wall shear stress*, $\mathrm{Ca} = \eta U_b/\gamma = 2\,\mathrm{We}/\mathrm{Re}$ is the Capillary number, $\Delta\tilde{p}^H = 8\,\tilde{L}_{\mathrm{UD}}$ is the nondimensional pressure drop over the nozzle in case of homogeneous Poiseuille flow inside the nozzle, and $\tilde{\tau}_{xr}^H|_{\tilde{r}=1} = -4$ is the corresponding nondimensional wall shear stress. Note that $\Delta\tilde{p}^H = -2(\tilde{\tau}_{xr}^H|_{\tilde{r}=1})\tilde{L}_{\mathrm{UD}}$ is the nondimensional force balance between the driving pressure gradient and the wall shear stress for homogeneous Poiseuille flow.

The advantage of defining $\tilde{P}_{\mathrm{exc}}$ and $\tilde{T}_{\mathrm{exc}}$ in this manner is that they describe the influence of the perturbation flow within the nozzle at finite Re with respect to the case of homogeneous Poiseuille flow expected for very high Re. As will be discussed later, this will enable us to model $\tilde{T}_{\mathrm{exc}}$ using results from the boundary-layer analysis of Goren [13]. Interestingly, the excess wall pressure drop relates also to the so-called *nozzle exit correction*, defined by Mitsoulis *et al.* [20] as $n_{\mathrm{ex}} = (\Delta\tilde{p}_w - \Delta\tilde{p}^H)/(-2\tilde{\tau}_{xr}^H|_{\tilde{r}=1})$, according to

$$n_{\mathrm{ex}} = \tilde{P}_{\mathrm{exc}}/16\,. \tag{17}$$

B. Cubic equation for jet contraction ratio

Equation (15) can be rearranged into a cubic equation in χ, given by

$$A\chi^3 + B\chi^2 + C\chi + D = 0, \quad A = \frac{2}{\mathrm{Ca}}, \quad B = \frac{4}{3}\mathrm{Re} + \tilde{K} - \frac{2}{\mathrm{Ca}}(\cos\varphi + \tilde{R}_i''(0)\cos^3\varphi), \quad C = 0,$$
$$D = -\mathrm{Re}. \tag{18}$$

Provided that gravity effects are negligible, the jet contraction ratio thus solely depends on Re and Ca.

C. Limiting jet behavior

From Eq. (15), or Eq. (18) alternatively, some interesting insights can be obtained of the limiting jet behavior in specific flow regimes. Below we will discuss six limiting cases.

1. Inertial regime

In the limit of high Reynolds number, Re $\gg 1$, and high Weber number, We $\gg 1$, the right-hand side is equal to zero, and Harmon's result [5] is again retrieved for the *inertial regime*: $\chi = \sqrt{3}/2$. In this limit, the integral momentum flux at the nozzle exit is equal to the integral momentum flux upstream of the nozzle, $\dot{M}_0 = \dot{M}_{\mathrm{UD}}$, which follows from Eq. (6) and considering that the sum of the terms on the right-hand side of this equation is zero for homogeneous Poiseuille flow within the entire nozzle.

2. Viscous regime

In the limit of very high viscosity, Re $\ll 1$, and high Capillary number, Ca $\gg 1$, the integral momentum balance is dominated by the viscous force on the right-hand side of Eq. (15). This is the *viscous regime*. Requiring that $\tilde{K} = 0$ for equilibrium, we find that the wall pressure drop along the nozzle has to balance the integral wall shear stress:

$$\tilde{p}|_{\tilde{x}=-\tilde{L}_{\mathrm{UD}}} - \tilde{p}_{\mathrm{atm}} = -2\int_{-\tilde{L}_{\mathrm{UD}}}^{0} \tilde{\tau}_{xr}|_{\tilde{r}=1} d\tilde{x}. \tag{19a}$$

Similarly, based on Eq. (6) for the flow within the nozzle, it is required that

$$\tilde{p}|_{\tilde{x}=-\tilde{L}_{\mathrm{UD}}} - 2\int_{0}^{1} \tilde{p}|_{\tilde{x}=0}\, \tilde{r}\, d\tilde{r} = -2\int_{-\tilde{L}_{\mathrm{UD}}}^{0} \tilde{\tau}_{xr}|_{\tilde{r}=1} d\tilde{x}. \tag{19b}$$

Combining the above two equations, we find that in the viscous regime the pressure at the nozzle exit plane has to obey the following condition:

$$2\int_{0}^{1} \tilde{p}|_{\tilde{x}=0}\, \tilde{r}\, d\tilde{r} = \tilde{p}_{\mathrm{atm}}. \tag{20}$$

This specific case has been simulated by Mitsoulis *et al.* [20]. Indeed, relative to the atmospheric pressure, their Fig. 16 indicates a reduced pressure at the nozzle lip and an elevated pressure in the core, which we attribute to the effect of a tensile and a compressive axial viscous stress in the lip and the core region, respectively. By substituting the above pressure condition at the nozzle exit into the nondimensional form of Eq. (10) and multiplying this equation with Re, it is found that the left and the right-hand side of the resulting equation are equal to zero. Thus, the pressure condition is also consistent with equilibrium for the flow downstream of the nozzle, as should be.

We note that $\dot{M}_p \neq \dot{M}_0 \neq \dot{M}_{\mathrm{UD}}$ in the viscous regime as pressure and viscous forces will adjust the velocity distribution around the nozzle exit region till a new equilibrium is achieved sufficiently far downstream of the nozzle. Finally, we remark that from the integral momentum balance no explicit equation can be obtained for the jet contraction ratio in this regime. Numerical simulations by Mitsoulis *et al.* [20] and Georgiou and Boudouvis [21] indicate that $\chi \approx 1.127$ for Re $= 0$ and Ca $\to \infty$, which agrees well with the value of $\chi \approx 1.135$ measured by Batchelor *et al.* [6] considering the accuracy of their measurements.

3. Surface-tension dominated regime

For very low Weber number, We $\ll 1$, and very low Capillary number, Ca $\ll 1$, the integral momentum balance is dominated by the capillary force on the right-hand side of Eq. (15). This is the *surface-tension dominated regime*. As we are seeking for an equilibrium solution, we require that We $\cdot \tilde{F}_{\mathrm{cap}} = 0$ in this case and that the interface curvature is constant along the jet, as otherwise the axial pressure gradient within the jet would become unbounded for We $\to 0$:

$$\chi = \cos\varphi + \tilde{R}_i''(0)\cos^3\varphi, \tag{21a}$$

$$\frac{1}{\tilde{R}_i\tilde{R}_i'}\frac{d}{d\tilde{x}}\left(\frac{\tilde{R}_i}{\sqrt{1+\tilde{R}_i'^2}}\right)=\frac{1}{\chi}, \tag{21b}$$

where the right-hand side of Eq. (21b) is the nondimensional curvature at $\tilde{x}=\tilde{L}_P$. By multiplying Eq. (21b) with $\tilde{R}_i\tilde{R}_i'$, integrating to $\tilde{x}$ and evaluating the result at $\tilde{x}=\tilde{L}_P$, we find that $\tilde{R}_i/\sqrt{1+\tilde{R}_i'^2}-\tilde{R}_i^2/(2\chi)-(\chi/2)=0$ should hold along the jet. At the nozzle exit, this condition reduces to $\cos\varphi=\frac{1}{2}(\chi+\frac{1}{\chi})$. Since $\cos\varphi\leqslant 1$ must hold, the only permitted solution is that $\chi=1$ and therefore $\cos\varphi=1$. Equation (21a) then implies that $\tilde{R}_i''(0)=0$ and thus the jet has to take the form of a cylinder with a constant radius equal to the nozzle radius. Indeed, finite-element simulations of Mitsoulis *et al.* [20] at $\mathrm{Re}=0$ confirm the stiffening of the jet interface with decreasing Capillary number and $\chi=1.000$ at $\mathrm{Ca}=10^{-5}$. Finally, we remark that the jet in the surface-tension dominated regime is highly unstable, either due to a capillary-inertial instability for $\mathrm{Oh}\ll 1$ or a capillary-viscous instability for $\mathrm{Oh}\gg 1$, where $\mathrm{Oh}=\eta/\sqrt{\rho\gamma R}$ is known as the Ohnesorge number [30].

4. Inertial effects negligible

For the regime in which inertia is negligible, $\mathrm{Re}\ll 1$, Eq. (18) yields the following expression for the jet contraction ratio:

$$\chi\approx\cos\varphi+\tilde{R}_i''(0)\cos^3\varphi-\frac{\mathrm{Ca}}{2}\tilde{K}\quad(\mathrm{Re}\ll 1). \tag{22}$$

In the limit of $\mathrm{Ca}\to 0$ (the surface-tension dominated regime), $\chi\to 1$, while in the limit of $\mathrm{Ca}\to\infty$ (the viscous regime), $\chi\approx 1.13$. At finite values of Ca, the jet expansion will be in between these two limits. Simulations of Mitsoulis *et al.* [20] at $\mathrm{Re}=0$ show a monotonic variation of χ from 1 till 1.13 when gradually varying Ca from a very small till a very large value.

5. Viscous effects negligible

For the regime in which viscous effects are negligible, $\mathrm{Re}\gg 1$, the following implicit relation can be derived from Eq. (18) for the jet contraction ratio:

$$\chi\approx\frac{\frac{1}{2}\sqrt{3}}{\sqrt{1+\frac{3}{4\mathrm{We}}(\chi-\cos\varphi-\tilde{R}_i''(0)\cos^3\varphi)}}\quad(\mathrm{Re}\gg 1). \tag{23}$$

For $\mathrm{We}\gg 1$ and considering that $\cos\varphi\approx 1$, this expression is approximately equal to $\chi\approx\frac{1}{2}\sqrt{3}(1+\frac{1}{20\,\mathrm{We}}[1+7.5\,\tilde{R}_i''(0)])$. This is equal to the approximation given by Sevilla [31] except for the additional inclusion of the axial curvature term here. Since $\tilde{R}_i''(0)>0$, it can be deduced from this that $\chi>\frac{1}{2}\sqrt{3}$ at finite We and that the effect of surface tension scales with $1/\mathrm{We}$ for sufficiently high We. For $\mathrm{We}\to 0$ (surface-tension dominated regime), it follows from Eq. (23) that $\chi\to 1$, which originates from stiffening of the jet interface as discussed before. Thus, we can conclude that surface tension is responsible for less contraction when $\mathrm{Re}\gg 1$. This theoretical result is confirmed by finite-element simulations of Haustein *et al.* [9] at $\mathrm{Re}=200$, showing less contraction for $\mathrm{We}=5$ ($\mathrm{Ca}=0.05$) as compared to $\mathrm{We}=\infty$.

6. Surface tension negligible

Finally, for the regime in which surface tension is negligible, $\mathrm{Ca}\gg 1$, Joseph [22] proposed the following correlation for $\tilde{K}$, valid for $\mathrm{Re}\gtrsim 10$:

$$\tilde{K}\approx -K_1\mathrm{Re}^{1/3}\quad(\mathrm{Ca}\gg 1,\ \mathrm{Re}\gtrsim 10), \tag{24}$$

where $K_1 \approx 1.97$ is a constant determined from a fit with experimental data of Goren and Wronski [10]. From Eq. (18) it then follows that the jet contraction ratio is given by

$$\chi \approx \frac{\frac{1}{2}\sqrt{3}}{\sqrt{1 - 1.48\,\mathrm{Re}^{-2/3}}} \quad (\mathrm{Ca} \gg 1,\ \mathrm{Re} \gtrsim 10). \tag{25}$$

By construction, this equation yields $\chi = 1$ for $\mathrm{Re} = 14.4$, as this was used to determine the constant K_1 by Joseph [22]. For $\mathrm{Re} \gtrsim 10$, Eq. (25) agrees well with experimental data for the contraction ratio from Middleman and Gavis [4], Goren and Wronski [10], and Gavis and Modan [7] for long nozzle lengths. Notice from Eq. (25) that viscous forces are responsible a lesser contraction of the jet at finite Re with respect to the high-Re limit of $\sqrt{3}/2$ and responsible for expansion of the jet when $\mathrm{Re} < 14.4$.

D. Influence of gravity

If gravity were included in the integral momentum balance, then this would constitute an additional force on the right-hand side of Eq. (15) equal to

$$\tilde{F}_{\mathrm{grav}} = \frac{1}{\mathrm{Fr}^2}\left[\frac{V_{\mathrm{jet}}}{\pi R^3} + \frac{L_{\mathrm{UD}}}{R}\right], \tag{26}$$

where $\mathrm{Fr} = U_b/\sqrt{gR}$ is the Froude number and $V_{\mathrm{jet}} = \int_0^{L_P} \pi R_i^2 dx$ is the jet volume between $x = 0$ and $x = L_P$. Note that the gravity force increases with increasing jet volume, indicating continuous stretching and thinning of the jet with downstream distance from the nozzle exit. Strictly speaking, when the gravity force is significant, the jet will therefore never reach an equilibrium radius.

Using the above expression for the gravity force, we can now assess the conditions under which gravity can be ignored by comparing the gravity force with the other terms in Eq. (15). Provided that surface tension has at most a minor influence, we expect that $V_{\mathrm{jet}}/(\pi R^3) + L_{\mathrm{UD}}/R = O(1)$ for $\mathrm{Re} \lesssim O(1)$ and $V_{\mathrm{jet}}/(\pi R^3) + L_{\mathrm{UD}}/R \propto \mathrm{Re}$ for $\mathrm{Re} \gg 1$ based on $L_p/R \propto \mathrm{Re}$ as shown in the next section. For both the viscous and the inertial regime, gravity can then be ignored when $\mathrm{Re}/\mathrm{Fr}^2 \ll 1$ or, alternatively, when $\rho g R/(\eta U_b/R) \ll 1$.

III. NUMERICAL METHOD AND COMPUTATIONAL SETUP

To analyze the influence of the Reynolds number on the jet behavior in more detail, we made use of the CFD finite-volume solver OpenFOAM [25] (version 6) and the rheoTool extension [32] to simulate this problem. The solver rheoInterFoam [33] uses an algebraic volume-of-fluid (VOF) method [34] for simulating two-phase flows with non-Newtonian properties for both phases. In the present study, both phases are Newtonian, with the density and the dynamic viscosity of the ambient gas set to very small values to ensure negligible dynamic effects from the ambient gas on the jet flow: $\rho_a/\rho = 5 \times 10^{-3}$ and $\eta_a/\eta = 10^{-7}$, respectively.

The incompressible Navier-Stokes equations were solved in cylindrical coordinates for the computational flow domain shown in Fig. 2. The nozzle wall was modeled as an infinitely thin wall with zero thickness. The simulations were 2D, assuming axisymmetry of the flow in the azimuthal direction. The simulations were carried out in a time-dependent fashion with a first-order implicit Euler scheme and ran until the flow was fully developed. The time step was dynamically adjusted according to a maximum Courant number of 0.2 to ensure numerical stability. A computational mesh of 116 000 cells was used to resolve the flow. Mesh refinement was applied near the nozzle wall and around the nozzle exit plane; see Fig. 3. Along the centerline of the jet, the axial dimension of the grid cells varied from $\Delta x/R = 2.94 \times 10^{-3}$ at the nozzle exit till $\Delta x/R = 8.76 \times 10^{-2}$ at the right domain boundary. At the nozzle exit, the radial dimension of the grid cells varied from $\Delta r/R = 4.25 \times 10^{-2}$ at the centerline till $\Delta r/R = 1.7 \times 10^{-3}$ at the nozzle lip.

A symmetry boundary condition was used for the centerline. A no-slip condition was imposed at BD, the nozzle wall; see Fig. 2. A parabolic Poiseuille flow was imposed at AB, the upstream

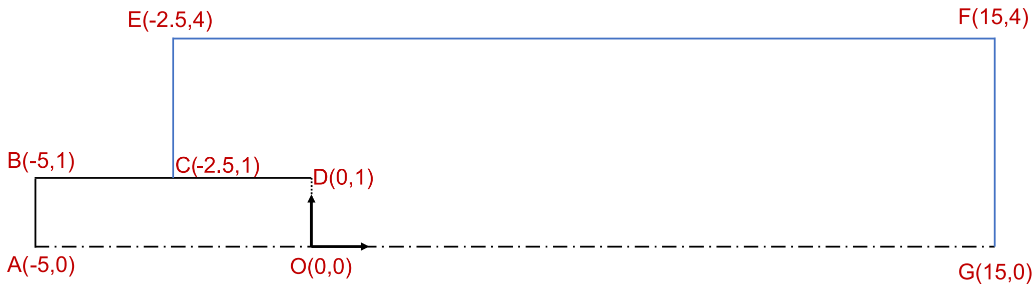

FIG. 2. Computational setup used to simulate the flow illustrated in Fig. 1. The numbers between brackets denote the spatial coordinates $(\tilde{x}, \tilde{r})$ normalized by the nozzle radius, where (0,0) denotes the origin located at the center of the nozzle exit plane.

entrance of the nozzle. To ensure a pinned contact line at the sharp-edged nozzle lip, a zero value for the VOF was imposed at CD, the outer wall of the nozzle, such that contact with the ambient gas was enforced. The domain boundaries CE, EF, and FG were placed sufficiently far from the nozzle exit to prevent any influence of these boundaries on the jet development. At CE and EF, the boundary conditions were a zero value for the pressure (i.e., the pressure of the ambient gas in the far field was effectively set to zero, $p_{\text{atm}} = 0$), a zero normal gradient for the velocity and a zero value for the VOF. At FG, the boundary conditions were a zero normal gradient for both the pressure, the velocity and the VOF. Note that the zero normal gradient for the pressure allows the pressure to vary over the jet interface at FG.

As initial flow condition, a straight liquid jet was prescribed with the same radius as the nozzle, and a Poiseuille (parabolic) profile was prescribed for the liquid velocity, both inside the nozzle and in the jet. The velocity of the ambient gas was set to zero. The simulations were run until convergence was reached for the jet shape and the velocity distribution.

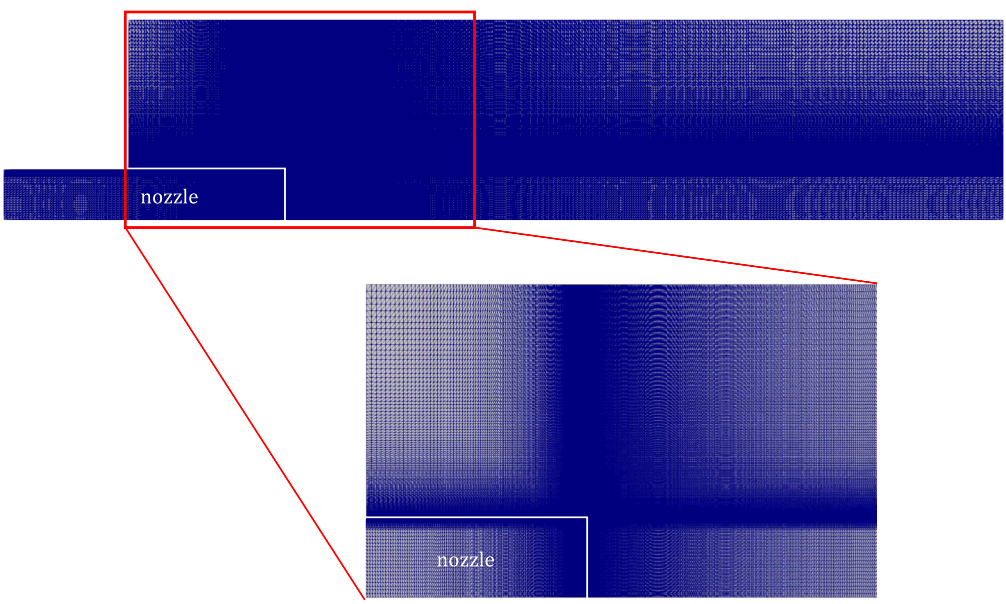

FIG. 3. Computational mesh used for the simulations.

TABLE I. Governing dimensionless numbers of the simulated cases, based on the experiments of Goren and Wronski [10] using glycerol-water mixtures and a nozzle with radius $R = 0.905\,\mathrm{mm}$. The Weber number is computed from $\mathrm{We} = \frac{1}{4}\mathrm{Re}^2/(S/\chi)$ with $S = \rho\gamma R_\infty/\eta^2 \approx 0.3$ is the value of the surface-tension parameter listed in Table 1 of Goren and Wronski [10]. The Capillary number was computed from their data according to $\mathrm{Ca} = \frac{1}{2}\mathrm{Re}/(S/\chi)$. Finally, the Froude number was computed from $\mathrm{Fr} = \mathrm{Re}/\sqrt{4\,(S/\chi)\,\mathrm{Bo}}$ with $\mathrm{Bo} = \rho g R^2/\gamma \approx 0.159$ the Bond number computed from the reported data and using $g = 9.8\,\mathrm{m/s^2}$ for the gravitational acceleration.

Case	$\mathrm{Re} = \frac{\rho U_b 2R}{\eta}$	$\mathrm{We} = \frac{\rho U_b^2 R}{\gamma}$	$\mathrm{Ca} = \frac{\eta U_b}{\gamma}$	$\mathrm{Fr} = \frac{U_b}{\sqrt{gR}}$
1	4.2	16.1	7.7	10.1
2	7.2	45.8	12.7	17.0
3	10.1	88.5	17.5	23.6
4	11.8	118.2	20.0	27.3
5	14.0	164.2	23.5	32.1
6	14.8	182.0	24.6	33.8
7	16.6	225.6	27.2	37.7
8	18.0	262.9	29.2	40.7
9	24.0	458.6	38.2	53.7
10	47.4	1733.8	73.2	104.4

We conducted a total of 10 simulations. The dimensionless numbers of the simulations are listed in Table I and were chosen after the experiments reported by Goren and Wronski [10]. This serves both to validate the present simulations with available experimental data for the jet shape and to use the simulation data for an in-depth study of the flow dynamics. Notice that $\mathrm{We} \gg 1$ and $\mathrm{Ca} \gg 1$ for most cases, suggesting negligible effects from surface tension on the jet; this will be analyzed in more detail later. Moreover, since $\mathrm{Re}/\mathrm{Fr}^2 \ll 1$ in all cases, gravity effects were likely negligible as well.

IV. RESULTS

A. Jet radius profile

Figure 4 depicts the results for the normalized jet radius as a function of the streamwise distance along the jet for all ten simulations. The jet radius is defined here as the radial position where the VOF function is equal to 0.5. The lines in Fig. 4 actually show the fits of a fifth-order trigonometric Fourier series to the VOF isolines for $x/R \in [0:5]$, but the VOF isolines and the Fourier fits are very close to each other. Only for the highest Reynolds number investigated, $\mathrm{Re} = 47.4$, small wiggles were observed in the VOF isoline. This is clearly a numerical artifact, but the wiggles are smoothed out by the Fourier series fit. A major advantage of the Fourier series fit is the possibility to obtain the curvature of the jet interface from the fit in an accurate analytic fashion.

The jet radius profiles generally agree well with the experimental data of Goren and Wronski [10] and Gear *et al.* [11], also taking into account the typical error margins indicated in the last-mentioned reference. It should be noted here that we multiplied the axial coordinate of the data of Goren and Wronski by a factor two, since they most likely used a normalization with the nozzle diameter instead of the nozzle radius indicated in their Fig. 2. The same correction to their data was also applied previously by Omodei [23] and Gear *et al.* [11]. Furthermore, Goren and Wronski reported a value of approximately 0.3 for their surface-tension parameter, $S = \rho\gamma R_\infty/\eta^2$, which can be written as $S = \chi/\mathrm{Oh}^2$. Since Oh is a constant at constant temperature and χ varied between $\approx$0.925 and 1.095 (a variation of about 18%), we conclude that S was likely not constant in the experiments of Goren and Wronski. Nevertheless, as indicated in Table I, the Weber and the Capillary number are

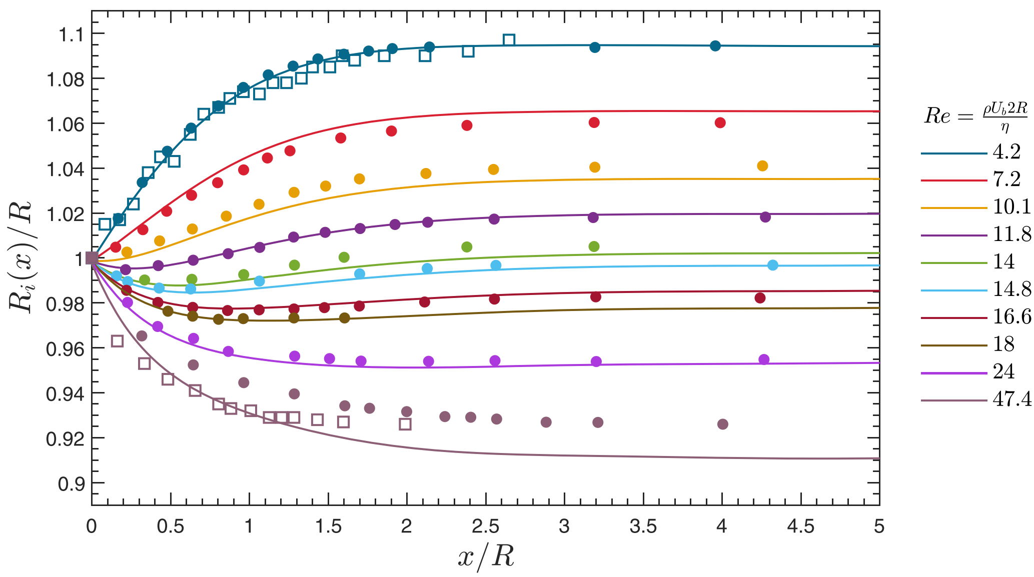

FIG. 4. Numerical results for the normalized jet radius as function of the normalized axial distance from the nozzle exit for the cases listed in Table I. The dots represent the experimental data from Goren and Wronski [10] with the axial distance corrected by a factor of two as discussed in the main text. The open square symbols are experimental data from Gear *et al.* [11] for Re = 4.09 and Re = 47.4, respectively.

generally large, suggesting that surface tension had only a minor influence on the jet behavior in their experiments anyway. This will be analyzed in more detail later.

The jet radius profiles obtained from our simulations are in very good agreement with the results from the finite-element simulations of Omodei [23], showing a similar deviation from the experimental data of Goren and Wronski [10] for Re = 7.2, 10.1, 14, and 47.4. The reason for the observed deviations from the experiments is unclear, but might originate from uncertainty in the experimental determination of the Reynolds number or other effects such as, for example, possible wetting of the outer nozzle perimeter in the experiments [9]. Notice that our result for Re = 47.4 agrees reasonably well with the experimental data from Gear *et al.* [11] for this Reynolds number.

Figure 4 shows that sufficiently far downstream, the jet expands for Re up to 14, while for Re of 14.8 and higher the jet contracts. This suggests a transition Reynolds number of Re ≈ 14.4 for the jet contraction behavior. Interestingly, for Reynolds numbers in the range of 10.1 until 14, the jet first contracts toward a local minimum and then expands to a value higher than the initial radius far downstream. A similar behavior is observed for Re = 14.8 until 24, though the jet does not expand beyond the initial value in these cases. For the highest investigated Reynolds number, Re = 47.4, the jet gradually contracts in a monotonic fashion till the equilibrium radius is reached. The jet contraction/expansion behavior for intermediate Reynolds numbers suggests competing influences of viscous stresses (responsible for jet expansion) and inertial flow effects (responsible for jet contraction).

B. Jet angle and curvature at nozzle exit

From the Fourier series fit of the jet radius profile, we analytically determined the angle φ of the jet interface with the nozzle wall from $\varphi = \arccos(1/\sqrt{1 + R_i'^2})$ at $x = 0$. Figure 5(a) shows φ as function of the Reynolds number. The angle decreases in a monotonic fashion from $\phi \approx 6^\circ$ at Re = 4.2 till $\phi \approx -10^\circ$ at Re = 47.4. Note that the contribution of the curved jet perimeter to

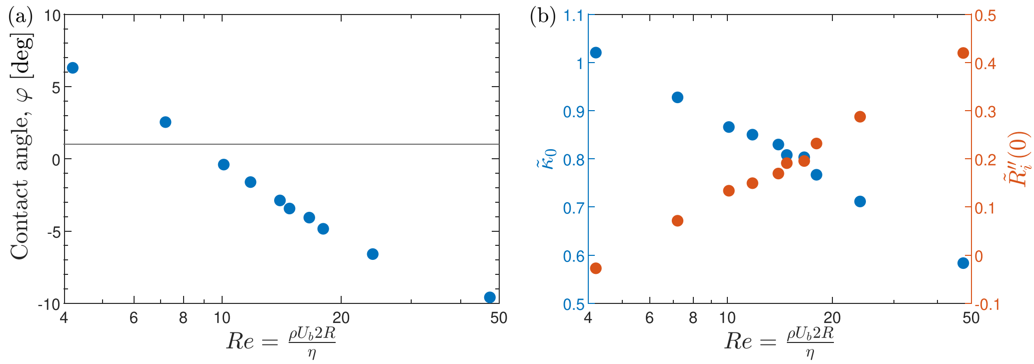

FIG. 5. (a) Angle, φ, of the jet interface at the nozzle exit with the nozzle wall as function of the Reynolds number. (b) Dimensionless second-order derivative of the jet radius, $\tilde{R}_0''$, and the dimensionless curvature, $\tilde{\kappa}_0 = \cos\varphi - \tilde{R}_0'' \cos^3\varphi$, at the nozzle exit as function of the Reynolds number.

the total jet curvature at $x = 0$ is equal to $(\cos\varphi)/R$, which varies only slightly, from $\approx 0.995/R$ till $\approx 0.985/R$, and is thus close to $1/R$ for the Re–range considered in our study.

In a similar fashion, we also determined the dimensionless second-order derivative of the jet radius, $\tilde{R}_0''$, and the dimensionless jet curvature, $\tilde{\kappa}_0 = \cos\varphi - \tilde{R}_0'' \cos^3\varphi$, at $x = 0$ from the Fourier series fit. Figure 5(b) shows $\tilde{R}_0''$ and $\tilde{\kappa}_0$ as function of the Reynolds number. The results show that $\tilde{R}_0''$ is negative, but nearly zero at $\mathrm{Re} = 4.2$, while positive for all larger Reynolds numbers investigated and monotonically increases with Re till a value slightly larger than 0.4 at $\mathrm{Re} = 47.4$. The nondimensional curvature, $\tilde{\kappa}_0$, is approximately equal to $1 - \tilde{R}_0''$ and hence gradually decreases with Re, varying from a value slightly larger than 1 at $\mathrm{Re} = 4.2$ till a value slightly less than 0.6 at $\mathrm{Re} = 47.4$.

C. Jet contraction ratio

In Fig. 6(a), results are presented for the jet contraction ratio. This has been obtained from the simulations in two different ways: (1) by directly measuring the equilibrium radius, R_∞, far

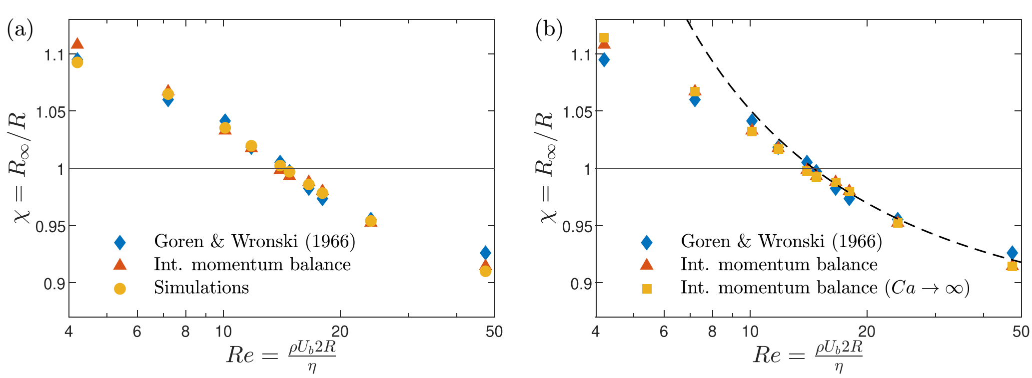

FIG. 6. (a) Jet contraction ratio, $\chi = R_\infty/R$, as function of Reynolds number. The data points show the results obtained from the simulations, the experiments of Goren and Wronski [10], and the contraction ratio computed from the integral momentum balance using Eq. (18). (b) Jet contraction ratio as function of Reynolds number. Symbols show the experimental data of Goren and Wronski [10] and the contraction ratio computed from Eq. (18) with and without the contribution from surface tension (using the actual value of Ca and $\mathrm{Ca} = \infty$, respectively). The dashed line shows the empirical correlation proposed by Joseph [22], Eq. (25), for $\mathrm{Re} \gtrsim 10$.

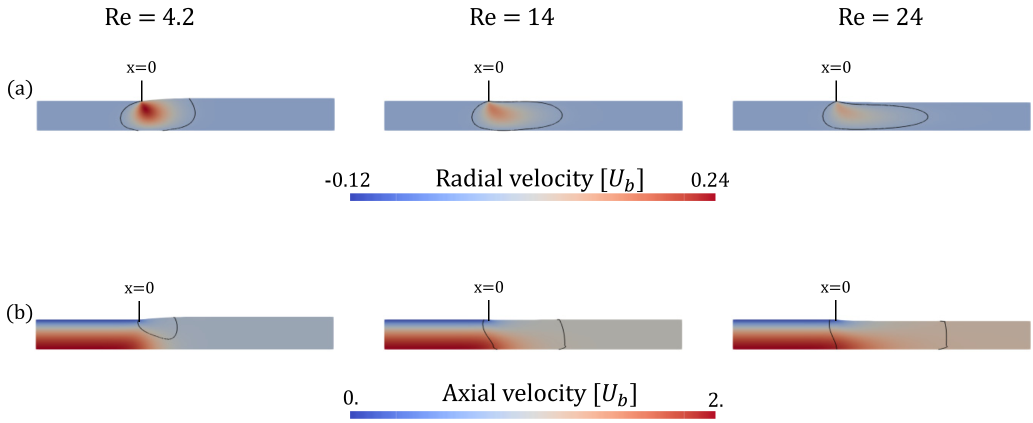

FIG. 7. Plots of the 2D flow field in the nozzle and the jet for Reynolds numbers of 4.2 (left), 14 (middle) and 24 (right). From top to bottom, the plots show (a) the magnitude of the radial velocity in units of U_b, and (b) the axial velocity in units of U_b. The contours in panels (a, b) show the isolines of, respectively, a radial velocity equal to 0.01 U_b and a zero pressure.

downstream of the nozzle, and (2) by computing χ from Eq. (18) with the coefficient B calculated numerically from the simulation data. The two methods give nearly the same value for the jet contraction ratio, which validates our theoretical derivation of the integral momentum balance from which χ was determined. Moreover, a good agreement is obtained with the experimental data from Goren and Wronski [10].

Figure 6(b) depicts the results for the jet contraction ratio computed from the integral momentum balance, Eq. (18), with and without the contribution from surface tension. To remove the *direct* effect of surface tension, we set the Capillary number simply to $\mathrm{Ca} = \infty$ in the cubic equation for χ instead of using the actual Ca value. It should be noted here that possible *indirect* effects of surface tension are not taken into account, as a change in the contraction ratio might have an effect on the flow upstream of the nozzle exit and will change the viscous contribution $\tilde{K}$ in the integral momentum balance accordingly. The results are again compared with the experimental data of Goren and Wronski [13]. This analysis indicates that surface tension has only a small influence on the jet behavior for $\mathrm{Re} = 4.2$, while it is negligible for the higher Reynolds numbers as already anticipated based on the corresponding values for the Capillary number and the Weber number in Table I. At $\mathrm{Re} = 4.2$, surface tension is responsible for a slightly reduced expansion of the jet, in line with the stiffening of the jet interface by surface tension as discussed in Sec. II.

The dashed line in Fig. 6(b) shows the correlation for the jet contraction ratio proposed by Joseph [22], given by Eq. (25). The correlation provides a good fit with the experimental data down to $\mathrm{Re} = 11.8$, below which the jet contraction ratio levels off to a value of approximately 1.13 at $\mathrm{Re} = 0$ [6,20], while Joseph's correlation diverges toward infinity for $\mathrm{Re} \to 0$. The deviation of the correlation from the experiments and simulations at low Re is clearly a viscous effect, since we found that the effect of surface tension is small for $\mathrm{Re} = 4.2$ and negligible at the higher Reynolds numbers.

D. Two-dimensional flow field

Figure 7 depicts the spatial distribution of the radial and the axial velocity within the nozzle and the jet for $\mathrm{Re} = 4.2$, 10.1 and 24, corresponding to an expanding, contracting/expanding and contracting jet, respectively. The radial velocity is strongest near the nozzle exit plane. The contours in Fig. 7(a) show isolines of a radial velocity equal to 0.01 U_b. Within the region enclosed by the isolines, the radial velocity is positive and thus directed outwards, while the radial velocity is close

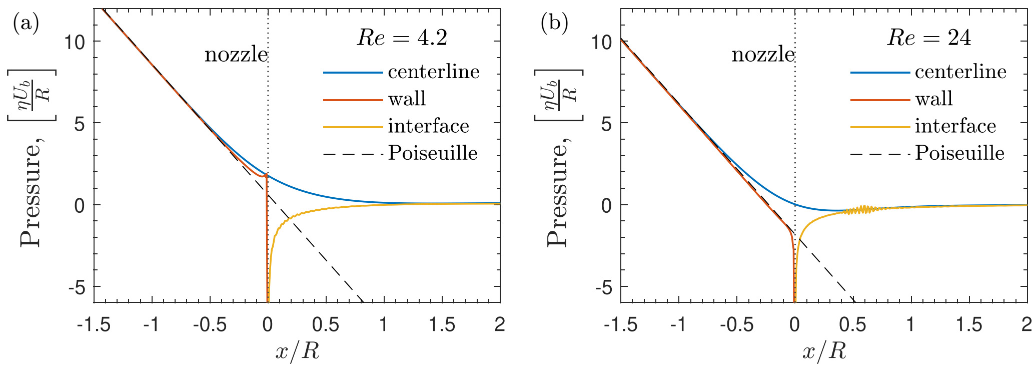

FIG. 8. One-dimensional pressure distributions at the nozzle wall, the centerline, and the jet interface for (a) Re $= 4.2$ and (b) Re $= 24$. The pressures are expressed in units of $\eta U_b/R$. The dashed line denotes the linear variation in the pressure according to homogeneous Poiseuille flow.

to zero almost everywhere outside this region. The positive radial velocity at the nozzle exit plane can be explained from the increase in the axial velocity near the nozzle lip due to the transition from stick at the wall to slip at the jet interface; see Fig. 7(b). Mass conservation dictates that the increase in axial velocity near the nozzle lip must be accompanied by a decrease in the axial velocity in the core, as visible from Fig. 7(b), and a radially outward flow from the core toward the nozzle lip. Normalized with U_b, the radial velocity perturbations decrease in magnitude with increasing Reynolds number and spread out further downstream related to streamwise advection by the higher axial velocity. The solid lines in Fig. 7(b) are isolines of zero pressure. Within the region enclosed by the isolines, the pressure is negative. The negative pressure downstream of the nozzle lip is consistent with the local increase in the axial velocity due to the stick-slip transition and drives the radially outward flow from the core to the nozzle lip at the nozzle exit.

E. Pressure profiles

Figure 8 show the pressure variation along the centerline, the wall and the free surface of the jet, for Re $= 4.2$ (expanding jet) and Re $= 24$ (contracting jet). The pressure at the centerline smoothly varies across the nozzle exit, while the pressure distribution along the nozzle wall and the jet interface displays a singularity at the nozzle exit, related to the transition from stick to slip. Sufficiently far upstream and downstream of the nozzle exit plane, the pressure is uniform in the radial direction. Furthermore, sufficiently far upstream of the nozzle exit, the pressure varies with x according to the linear pressure profile for homogeneous Poiseuille flow, while the pressures at the centerline and the wall both deviate from that in the region near the nozzle exit. Near the exit within the nozzle, the pressure at the wall is lower than at the centerline for both Reynolds numbers. Thus, a radial pressure gradient exists, which drives the radially outward flow from the core toward the nozzle lip at the nozzle exit. Immediately downstream of the nozzle exit, the pressure at the jet interface is lower than the zero gas pressure in the far field outside the jet, while the pressure at the centerline is higher than the gas pressure. Finally, sufficiently far downstream, it follows from Eq. (7a) that the pressure within the jet is equal to $p_\infty = p_{\text{atm}} + \gamma/R_\infty$, thus slightly higher than the ambient gas pressure in the far field.

F. Centerline velocity

Figure 9 depicts the centerline velocity as function of the streamwise distance from the nozzle exit plane for each investigated Reynolds number. The velocity is normalized with the bulk velocity inside the nozzle, U_b. For all Reynolds numbers, the centerline velocity decreases monotonically

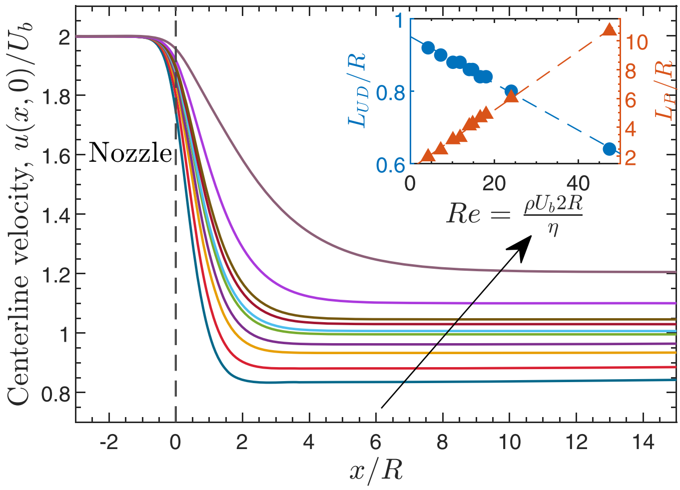

FIG. 9. Centerline velocity normalized by the bulk velocity upstream in the nozzle, $u(x, 0)/U_b$, as function of normalized streamwise distance from the nozzle exit plane, x/R. Lines represent the ten different Reynolds numbers considered in our study, see Table I, increasing in the direction of the arrow. The inset shows the upstream diffusion length, L_{UD}, and the downstream velocity relaxation length, L_P, as function of Reynolds number.

from a value of $u(x, 0)/U_b = 2$ at a distance of the order of one nozzle radius upstream of the nozzle exit plane to an equilibrium value of $U_\infty/U_b = 1/\chi^2$ sufficiently far downstream. At the highest Reynolds number, Re = 47.4, the equilibrium value is approximately 1.2. This is still quite a bit below the limiting value of 4/3 (≈ 1.33) in the inertial regime for very high Re, indicating that viscous effects are still significant at this Reynolds number.

The rapid decrease of the centerline velocity around the nozzle exit plane implies the local presence of a compressive axial viscous stress, $\tau_{xx} = 2\eta\partial u/\partial x < 0$. Mass conservation dictates that this must be accompanied by a radially outward velocity gradient, as indeed observed from Fig. 7(a), and hence the local presence of an tensile radial viscous stress at the centerline, $\tau_{rr} = 2\eta\partial v/\partial r > 0$ with v denoting the radial velocity. The reverse situation occurs near the nozzle lip, where $\tau_{xx} > 0$ immediately downstream of the nozzle lip. In this case, mass conservation requires that $\partial(rv)/\partial r < 0$ immediately downstream of the nozzle lip. For sufficiently small Re, the jet expands in the downstream direction, so $v > 0$ near the nozzle edge. Combined with $\partial(rv)/\partial r < 0$, this implies the local presence of a compressive radial viscous stress, $\tau_{rr} < 0$; this can also be directly inferred from the radial velocity field near the jet interface for Re = 4.2 shown in Fig. 7(a). From Eq. (12a) we then find that the normal viscous stress acting on the free surface is negative immediately downstream of the nozzle lip, $(\mathbf{n} \cdot \boldsymbol{\tau} \cdot \mathbf{n})_i < 0$. Furthermore, from Eq. (7a) it can be deduced that for sufficiently low Re and when surface tension is negligible, the pressure immediately downstream of the nozzle edge has to be smaller than the atmospheric pressure outside the jet to satisfy the normal-stress balance at the jet interface. This is also observed in our simulations; see the pressure contours in Fig. 7(b). This low pressure downstream of the nozzle lip and the corresponding radial pressure gradient is compatible with the radially outward flow ($v > 0$) from the core toward the nozzle lip at the nozzle exit.

The above reasoning provides a conceptual explanation for the jet expansion observed for low Re. The change from a no-slip to a free-slip condition for the flow leaving the nozzle, generates axial viscous stresses, which through mass conservation are responsible for a compressive normal viscous stress at the jet interface, by which the interface is pushed outwards to maintain normal-stress equilibrium with the ambient gas at atmospheric pressure. At higher Re, inertial effect come into play and the jet undergoes a contraction when leaving the nozzle. The conceptual picture for the Stokes regime breaks down in this case as the flow acceleration near the nozzle lip and the flow deceleration in the core region will strongly influence the flow dynamics. Compared to the dynamic pressure at the interface, which is on the order of $\frac{1}{2}\rho u_i^2$ with u_i the axial slip velocity, the magnitude of the normal viscous stress at the interface is expected to rapidly decrease with Re. Thus, at high Re (i.e., in the inertial regime), the normal viscous stress at the interface is expected to have a negligible effect on the contraction of the jet and, provided that We is high too (negligible surface tension), the pressure at the interface will be close to the atmospheric pressure when normalized by the dynamic pressure.

The compressive axial viscous stress near the center of the nozzle exit plane and the tensile axial viscous stress near the nozzle edge are responsible for a more blunted velocity profile immediately upstream of the exit plane with respect to parabolic Poiseuille flow. This will affect both the streamwise pressure gradient and the wall shear stress at the nozzle wall. To quantify the streamwise extent of the affected nozzle region, we define the "upstream diffusion length", L_{UD}, as the position $x = -L_{\mathrm{UD}}$ where the centerline velocity is within 0.2% of the centerline velocity of homogeneous Poiseuille profile. Similarly, we also introduce the "downstream velocity relaxation length" as the position $x = L_P$ where the centerline velocity and the velocity at the jet interface differ by less than 1% and a plug-flow condition is reached. The numerical results for L_{UD}/R and L_P/R are shown in the inset of Fig. 9 as function of Re. Interestingly, over the investigate Re range, the variation in the length scales is approximately linear in Re and given by, respectively:

$$L_{\mathrm{UD}}/R \approx -6.5 \times 10^{-3}\,\mathrm{Re} + 0.95, \tag{27a}$$

$$L_P/R \approx 0.2\,\mathrm{Re} + 1.13. \tag{27b}$$

While at the very low Reynolds numbers, the ratio L_{UD}/L_P is $O(1)$, the ratio quickly drops down with increasing Re and will eventually approach zero for high Re in the inertial regime. Note that Eq. (27a) predicts that $L_{\mathrm{UD}}/R = 0$ for $\mathrm{Re} \approx 146$, and since L_{UD} cannot be negative, this correlation cannot be used for Reynolds numbers beyond this value. Interestingly, at $\mathrm{Re} = 146$, Eq. (25) predicts that the value of the jet contraction ratio is within 3% of Harmon's theoretical high-Re limit of $\chi = \sqrt{3}/2$.

G. Flow behavior near nozzle exit

In Fig. 10, the centerline velocity is again depicted as a function of the streamwise distance, but now as the velocity difference with respect to the centerline velocity at the nozzle exit and normalized according to $(u(x,0) - u(0,0))/(2U_b - u(0,0))$. By definition, this normalized velocity difference is equal to 1 sufficiently far upstream of the nozzle exit plane and equal to 0 at the nozzle exit plane. Interestingly, Fig. 10 shows that the velocity profiles of all ten simulations collapse with each other for $x/R \lesssim 0.25$, indicating self-similar flow behavior:

$$\frac{u(x,0) - u(0,0)}{2U_b - u(0,0)} = f(x/R) \quad (x/R \lesssim 0.25), \tag{28}$$

where f is a nondimensional function that depends on x/R only, independent of the Reynolds number. Note that by definition $f(0) = 0$ and that $f(-L_{\mathrm{UD}}/R)$ is slightly less than one.

The inset in Fig. 10 shows the difference of the centerline velocity at the nozzle exit relative to the value expected for homogeneous Poiseuille flow and normalized according to $(2U_b - u(0,0))/(2U_b)$. For very high Re, the velocity difference should approach zero. For the investigated Re range, the normalized velocity difference at the nozzle exit plane appears to follow a power law as function of Re according to

$$\frac{2U_b - u(0,0)}{2U_b} \approx \alpha\,\mathrm{Re}^{-2/3}, \tag{29}$$

where $\alpha \approx 0.36$ is a constant obtained from fitting the power law with our data.

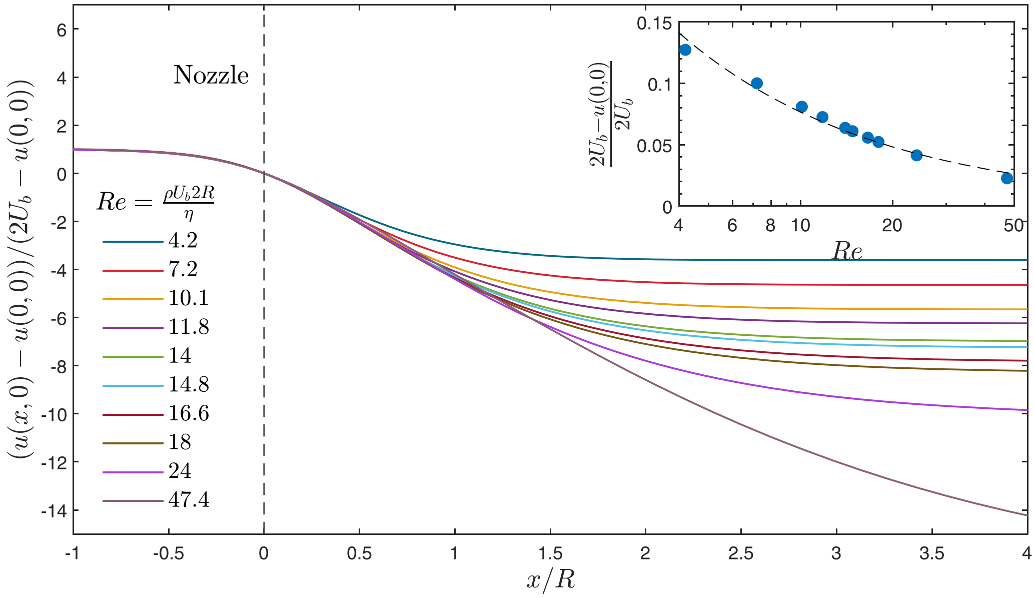

FIG. 10. Normalized centerline velocity difference, $f = (u(x,0) - u(0,0))/(2U_b - u(0,0))$, shown as function of x/R. The lines represent different Reynolds numbers. The inset shows the normalized centerline velocity difference at nozzle exit with respect to homogeneous Poiseuille flow, $(2U_b - u(0,0))/(2U_b)$, as function of Re.

Equation (29) can be combined with Eq. (28) to obtain the following relation for the centerline velocity:

$$u(x,0) \approx 2U_b[1 - \alpha\,\mathrm{Re}^{-2/3}(1 - f(x/R))] \quad (x/R \lesssim 0.25). \tag{30}$$

From this expression, we can also derive the following scaling relation for the axial viscous stress at the centerline:

$$\tau_{xx}(x,0) \approx 4\alpha\frac{\eta U_b}{R}\mathrm{Re}^{-2/3} f'(x/R) \quad (x/R \lesssim 0.25), \tag{31}$$

where $f' < 0$ is the derivative of f with respect to x/R and with a value of $O(-1)$; see Fig. 10.

An explanation for the observed scaling behavior for the centerline velocity and axial viscous stress can be found from the boundary-layer analysis of Goren [13]. For sufficiently high Re and assuming negligible effects from surface tension and gravity, and neglecting the interaction of the flow within the thin boundary layer at the jet perimeter with the flow in the jet core, Goren found the following scaling relations for the jet radius (R_i), the boundary-layer thickness along the curved interface (δ_{bl}), and the axial velocity at the jet interface near the nozzle exit (u_i):

$$\frac{R - R_i(x)}{R}, \quad \frac{\delta_{bl}}{R}, \quad \frac{u_i(x)}{U_b} \sim \left(\frac{x}{R}\frac{1}{\mathrm{Re}}\right)^{1/3}. \tag{32}$$

Note that $R_i'' \to \infty$ for $x \to 0$ according to Eq. (32), which is unphysical and will result in an infinite Laplace pressure from surface tension. Nonetheless, experiments by Goren and Wronski [10] showed that the jet radius near nozzle exit behaves indeed according to Eq. (32), albeit the results did not perfectly collapse onto each other and the constant prefactor was different from the prediction based on the boundary-layer analysis.

Mass conservation requires that the increase in the velocity at the jet interface near the nozzle edge must be accompanied by a decrease of the flow in the jet core. For a thin boundary layer, the

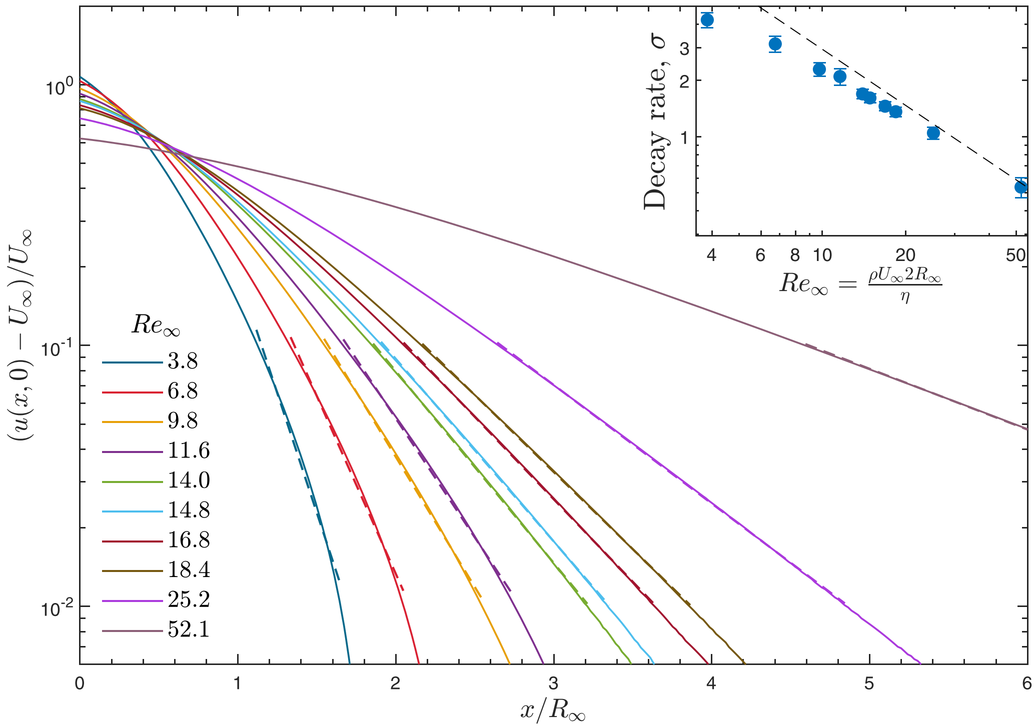

FIG. 11. Normalized centerline velocity difference relative to the uniform jet velocity at infinity, $(u(x,0) - U_\infty)/U_\infty$, shown as function of the normalized distance from the nozzle exit, x/R_∞. The lines represent different Reynolds numbers. The inset shows the exponential decay rate as function of $\mathrm{Re}_\infty = \rho U_\infty 2R_\infty/\eta$, obtained for the range of $(u(x,0) - U_\infty)/U_\infty \in [0.01 : 0.1]$ (dashed lines in main figure). Error bars show the standard deviation of the decay rate estimated from a least-squares fitting method. The dashed line in the inset is Bohr's theoretical result for high Reynolds number [10,12]: $\sigma = 29.36/\mathrm{Re}_\infty$.

following linearized equation can be derived from this for the velocity perturbation at the centerline:

$$\frac{u(x,0) - u(0,0)}{U_b} \sim -\frac{\delta_{bl} u_i}{R_i U_b} \sim -\mathrm{Re}^{-2/3}(x/R)^{2/3}. \tag{33}$$

The predicted scaling with $\mathrm{Re}^{-2/3}$ is confirmed by Eq. (30), from which it follows that $[u(x,0) - u(0,0)]/U_b = 2\alpha\,\mathrm{Re}^{-2/3} f(x/R)$. This also seems to suggest that $f(x/R) \sim -(x/R)^{2/3}$ at some distance near the nozzle exit.

H. Flow behavior in the far field

In Fig. 11, the centerline velocity is again plotted, but now the velocity difference with respect to the uniform jet velocity in the far field, U_∞, and normalized by the same velocity. The streamwise distance is normalized by the equilibrium radius of the jet in the far field, R_∞. A theoretical analysis by Goren and Wronski [10] showed that the velocity perturbations in the far field should exponentially decay to zero according to

$$\frac{u(x,0) - U_\infty}{U_\infty} \sim \exp(-\sigma\, x/R_\infty), \tag{34}$$

where σ is the exponential decay rate and which depends on the equilibrium Reynolds number, $\mathrm{Re}_\infty = \mathrm{Re}/\chi$. For $\mathrm{Re}_\infty \gtrsim 40$, Goren and Wronski found that $\sigma \approx 29.36/\mathrm{Re}_\infty$, a result first derived

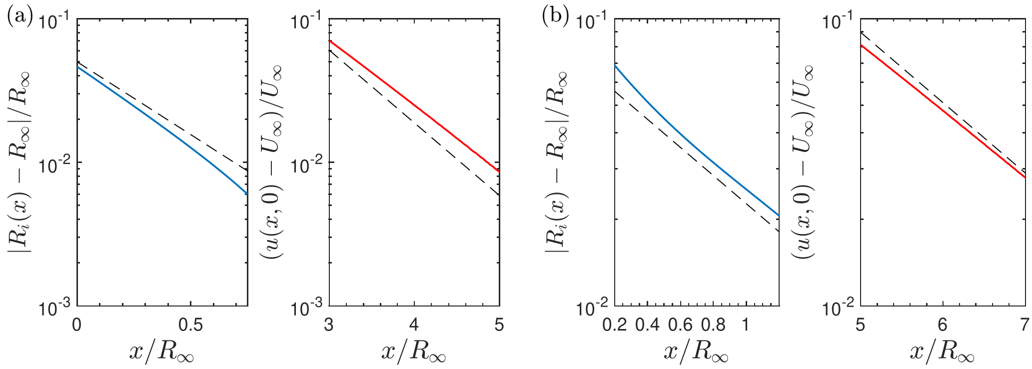

FIG. 12. Exponential decay of the jet radius and the jet centerline velocity toward their equilibrium values sufficiently far downstream of the nozzle exit, shown for (a) Re = 24 ($\mathrm{Re}_\infty = 25.2$), and (b) Re = 47.4 ($\mathrm{Re}_\infty = 52.1$). The dashed lines in the graphs for the jet centerline velocity correspond to an exponential decay rate of $\sigma = 29.36/\mathrm{Re}_\infty$ (Bohr's prediction [10,12]), while the dashed lines in the graphs for the jet radius correspond to a twice as high exponential decay rate of $\sigma = 58.72/\mathrm{Re}_\infty$.

by Bohr [12] (p. 298) for the related problem of viscous damping of axial velocity variations across a fluid cylinder with a constant radius. The results from our simulations confirm the exponential decay in the axial velocity perturbation in the far field. For the range of $(u(x,0) - U_\infty)/U_\infty \in [0.01 : 0.1]$, we determined the decay rate; see the dashed lines in Fig. 11. The inset shows the decay rate for all ten simulations as function of Re_∞. The decay rate monotonically decreases with Re_∞ and approaches Bohr's result for the highest Reynolds numbers investigated.

Assuming that the maximum velocity difference across the jet scales linearly with the velocity difference between the jet centerline and the equilibrium velocity in the far field and using the definition of the jet velocity relaxation length (L_P), it can be deduced from Eq. (34) that $L_p/R \sim \mathrm{Re}/\chi$ at sufficiently high Re. Since χ varies only weakly with Re at high Reynolds number, we thus find $L_p/R \sim \mathrm{Re}$ at sufficiently high Re, in agreement with the linear scaling of L_p/R with Re expressed by Eq. (27b).

For the highest two investigated Reynolds numbers, Fig. 12 compares the decay in the normalized jet radius with the decay in the normalized jet centerline velocity. Both show an exponential decay in x/R_∞, but the decay of the jet radius is much faster, as was already noticed by Duda and Vrentas [15] and Sevilla [31]. The exponential decay rate of the radius is approximately twice as high as the exponential decay rate of the centerline velocity and equal to $\sigma \approx 58.7/\mathrm{Re}_\infty$. This confirms what Goren and Wronski [10] reported about the exponential decay rate of the jet radius. As already suggested by them, higher-order terms in the series solution for the jet behavior in the far field probably cannot be neglected when considering the decay in the jet radius since the distance over which the decay takes place is short and on the order of R_∞ as observed from Fig. 12. Furthermore, nonlinear flow effects are nonnegligible close to the nozzle exit, contrary to what was assumed in the linear analysis of Goren and Wronski [10] for the jet behavior in the far field.

I. Viscous contribution to jet contraction ratio

Figure 13(a) shows the contributions from the excess wall pressure drop, $\tilde{P}_{\mathrm{exc}}$, and the excess integral wall shear stress, $\tilde{T}_{\mathrm{exc}}$, to the viscous term, $\tilde{K}$, in the coefficient B of the cubic equation for the contraction ratio; see Eq. (18). The values of $\tilde{K}$, $\tilde{P}_{\mathrm{exc}}$ and $\tilde{T}_{\mathrm{exc}}$ were computed from their definitions given by Eqs. (16a)–(16c).

Our results for $\tilde{K}$ agree well with the correlation proposed by Joseph [22] for Re $\gtrsim$ 10 given by Eq. (24). Our prefactor of $K_1 \approx 1.85$ is slightly smaller than the prefactor of $K_1 \approx 1.97$ proposed by Joseph, but falls within the uncertainty range of the experiments used by Joseph to fit his correlation.

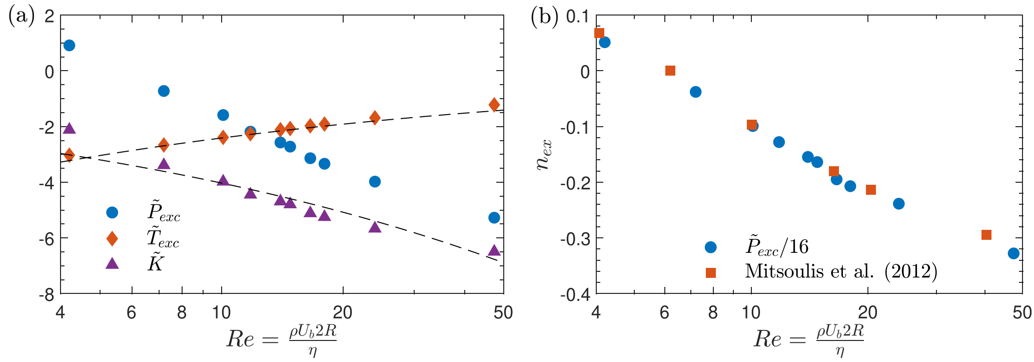

FIG. 13. (a) Contribution from the nondimensional excess wall pressure drop, $\tilde{P}_{\mathrm{exc}}$, and the nondimensional excess integral wall shear stress, $\tilde{T}_{\mathrm{exc}}$ to the nondimensional viscous force, $\tilde{K}$, shown as function of the Reynolds number. Dashed lines represent the correlations $\tilde{T}_{\mathrm{exc}} = -5.2\,\mathrm{Re}^{-1/3}$ and $\tilde{K} = -1.87\,\mathrm{Re}^{1/3}$. (b) Nozzle exit correction, $n_{\mathrm{ex}} = \tilde{P}_{\mathrm{exc}}/16$, as function of the Reynolds number. The symbols show the data from the present simulations and results from finite-element simulations of Mitsoulis *et al.* (their Fig. 5) [20].

For Re < 11.8, the contribution from the excess integral wall shear stress to $\tilde{K}$ is dominant over the contribution from the excess wall pressure drop, while the opposite holds for Re > 11.8.

The contribution from the excess wall pressure drop is positive at Re $= 4.2$, while negative for all larger Reynolds numbers in the investigated range. As discussed before, the excess wall pressure drop relates to the nozzle exit correction according to $n_{\mathrm{ex}} = \tilde{P}_{\mathrm{exc}}/16$; see Eq. (17). In Fig. 13(b) we compare the exit correction computed in this manner with the results from the finite-element simulations of Mitsoulis *et al.* [20] at zero surface tension (their Fig. 5) for the Re range considered in our study. The results are in good agreement with each other. This plot also suggests that for Re $\lesssim 6$ axial viscous stresses are responsible for an increase in the pressure drop within the nozzle, while for Re $\gtrsim 6$ the opposite holds, likely originating from inertial effects that start to dominate the pressure perturbation field within the nozzle at a higher Reynolds number.

Finally, the excess integral wall shear stress is always negative and appears to follow a power law in the Reynolds number according to $\tilde{T}_{\mathrm{exc}} \sim -\mathrm{Re}^{-1/3}$. This scaling can be explained from the boundary-layer theory of Goren [13], which shows that the perturbation velocity at the interface immediately downstream of the nozzle exit is proportional to $\mathrm{Re}^{-1/3}$; see Eq. (32). Although not considered in Goren's analysis, these perturbations are responsible for a tensile axial viscous stress that scales with $\mathrm{Re}^{-1/3}$. This in turn will lead to upstream velocity perturbations that will likely scale in the same manner and will cause an enhanced magnitude of the wall shear stress according to $(\tilde{\tau}_{xr} - \tilde{\tau}^{H}_{xr})_{\tilde{r}=1} \sim -\mathrm{Re}^{-1/3}$. As the flow perturbations extend within the nozzle over a streamwise distance on the order of the nozzle radius, see Eq. (27a), this suggests that $\tilde{T}_{\mathrm{exc}} \sim -\mathrm{Re}^{-1/3}$, which is indeed observed from Fig. 13(a). We note that this scaling law is not expected to hold in the limit of Re $\to 0$ as the boundary-layer theory of Goren holds only for sufficiently high Re. Since $\tilde{K} \to 0$ is required for equilibrium when Re $\to 0$, it should hold that $\tilde{T}_{\mathrm{exc}} \approx -\tilde{P}_{\mathrm{exc}}$ in this limit. The results from Mitsoulis *et al.* [20] suggests a limiting value of the exit correction of $n_{\mathrm{ex}} \approx 0.227$ and hence $\tilde{T}_{\mathrm{exc}} \approx -16\,n_{\mathrm{ex}} \approx -3.63$ is expected for Re $\to 0$. The observed power law for the excess integral wall shear stress, $\tilde{T}_{\mathrm{exc}} \approx -5.2\mathrm{Re}^{-1/3}$, for our range of investigated Re, is therefore expected to hold down to Re $\approx (3.63/5.2)^{-3} \approx 3$.

V. CONCLUSIONS AND DISCUSSION

We studied the influence of the Reynolds number on the behavior of a laminar axisymmetric jet of a Newtonian liquid issued from a long circular nozzle into a gaseous environment, with a focus on the transition from expanding to contracting liquid jets when the Reynolds number is gradually increased. An integral momentum balance was derived from the Navier-Stokes equations for the flow in both the nozzle and the jet. A detailed discussion was given of the forces appearing in this balance related to gravity, viscous effects and surface tension. A useful decomposition was made of the viscous force into a contribution from the excess wall pressure drop, which relates to the nozzle exit correction, and a contribution from the excess integral wall shear stress in the nozzle. When gravity effects are negligible, the flow behavior is governed by two dimensionless numbers: the Reynolds number, Re, and the Capillary number, Ca. Alternatively, either of the two numbers may be replaced by the Weber number, $\mathrm{We} = \mathrm{Ca} \cdot \mathrm{Re}/2$. The limiting behavior was analyzed theoretically for different cases such as the inertial regime ($\mathrm{Re} \gg 1$, $\mathrm{We} \gg 1$), the viscous regime ($\mathrm{Re} \ll 1$, $\mathrm{Ca} \gg 1$) and the surface-tension dominated regime ($\mathrm{Ca} \ll 1$, $\mathrm{We} \ll 1$). Surface tension is responsible for stiffening of the jet interface and tends to counteract any change of the jet radius from the nozzle radius. Viscous effects tend to expand the jet.

We presented results from numerical simulations of laminar liquid jets using the CFD finite-volume solver OpenFOAM. After the experiments of Goren and Wronski [10], ten cases were selected with the Reynolds number varying from 4.2 till 47.4. Our numerical results for the spatially varying jet radius are in good agreement with the experiments as well as with finite-element simulations reported by Omodei [23]. A reconstruction of the jet contraction ratio using the integral momentum balance, provided evidence that surface tension was responsible for a slightly reduced expansion of the jet at the lowest Reynolds number ($\mathrm{Re} = 4.2$) in the experiments of Goren and Wronski [13]. Our results indicate that the expansion of the jet at low Re originates from a radially outward flow and the accompanying compressive normal viscous stress at the jet interface immediately downstream of the nozzle exit. Consistent with the radially outward flow near the nozzle exit, is also the presence of an excess integral wall shear stress within the nozzle, which is responsible for a negative viscous force acting on the flow in the nozzle. The associated reduction of the integral momentum flux requires an expansion of the jet to maintain the integral momentum balance for the entire flow in the nozzle and the jet.

Self-similarity was observed for the axial velocity at the centerline within the nozzle and slightly outside the nozzle up to a distance of approximately $0.25\,R$ downstream of the nozzle exit. The self-similar solution implies that the associated compressive axial viscous stress at the centerline scales with $\mathrm{Re}^{-2/3}$ when normalized with $\eta U_b/R$. The stress reduces to zero in the upstream direction at a distance of $O(R)$ and this distance linearly decreases with Re over the investigated Re range. The stick-slip transition at the nozzle exit is responsible for an increment in the wall shear stress within the nozzle that scales with $\mathrm{Re}^{-1/3}$ when normalized with $\eta U_b/R$, implying self-similar behavior for the axial velocity near the nozzle wall as well. The observed scaling of the flow inside the nozzle is explained from the axial viscous stresses imposed by the self-similar boundary-layer flow along the jet interface downstream of the nozzle exit. Although not explicitly accounted for in Goren's theoretical analysis [13], the boundary-layer flow is responsible for a tensile axial viscous stress along the nozzle wall and, as dictated by mass conservation, a compressive axial viscous stress at the centerline, resulting in the observed scaling behavior with $\mathrm{Re}^{-1/3}$ and $\mathrm{Re}^{-2/3}$, respectively.

Sufficiently far downstream of the nozzle exit, the centerline velocity was found to exponentially decay toward the equilibrium solution, in agreement with the theoretical prediction of Goren and Wronski [10]. The decay rate decreases with Re. For $\mathrm{Re} = 24$ and 47.4, the decay rate was in good agreement with Bohr's predicted decay rate [10,12] of radial velocity differences in a jet with a constant radius and where axial viscous diffusion was ignored. The exponential decay rate is also consistent with the observed linear scaling of the velocity relaxation length with Re. The jet radius decays approximately twice as fast to the equilibrium radius as compared to the decay of the centerline velocity. This was already noticed by Goren and Wronski [10], which they attributed to the effect of higher-order terms in the series solution for the perturbation stream function. Nonlinear effects, which are not included in their theory for the behavior of the jet in the far field, are also nonnegligible near the nozzle exit.

The normalized viscous force, $\tilde{K}$, in the integral momentum balance for the nozzle and jet flow, scales with $-\mathrm{Re}^{1/3}$ for $\mathrm{Re} \gtrsim 10$, in agreement with the scaling originally proposed by Joseph [22]. The decomposition of the normalized viscous force into a nondimensional excess wall pressure drop and a nondimensional excess integral wall shear stress, shows that the contribution from the excess integral wall shear stress dominates over the contribution from the excess wall pressure drop for Re $\lesssim 12$, while the opposite holds for Re $\gtrsim 12$. The nondimensional excess integral wall shear stress scales with $-\mathrm{Re}^{-1/3}$ for the investigated Re–range. The excess wall pressure drop is positive for Re $\lesssim 6$, while negative for Re $\gtrsim 6$. We argued theoretically that for Re $\to 0$ (viscous regime), the excess integral wall shear stress and excess wall pressure drop should be equal and opposite to each other, as flow equilibrium requires that $\tilde{K} = 0$ in this limit. Furthermore, using results from Mitsoulis *et al.* [20] for the nozzle exit correction, we estimated that the observed scaling of the nondimensional excess integral wall shear stress with $-\mathrm{Re}^{-1/3}$ holds only for Re $\gtrsim 3$, while for Re $\to 0$ the excess integral wall shear stress will approach a constant value independent of the Reynolds number.

For future research, it is recommended to extend the theoretical boundary-layer analyses of Goren [13], Duda and Vrentas [15], and Philippe and Dumargue [16] to include the interaction with the flow within the nozzle. In particular, near the nozzle exit, axial diffusion cannot be ignored, as was already noted by Vrentas and Vrentas [35]. For the two-dimensional, planar case, this was already done by Tillett [14], using the method of matched asymptotic expansions and ignoring surface tension. However, to our knowledge, such an analysis has not yet been performed for the axisymmetric case. This could provide further insight into the self-similar flow behavior inside the nozzle, and provide theoretical support for the observed scaling behavior of, e.g., the excess integral wall shear stress with Re. As the boundary-layer analysis breaks down at low Re, it is also worth studying the transition from the inertial to the viscous regime when Re is gradually reduced and the according change in the scaling behavior of the flow. For Re $\to 0$, our theoretical analysis of the integral momentum balance suggests that the normalized viscous force should approach zero, $\tilde{K} \to 0$, which suggests that $\tilde{P}_{\mathrm{exc}} = -\tilde{T}_{\mathrm{exc}}$ in this limit.

In our study, we considered a Newtonian fluid. The theoretical derivation of the integral momentum balance can be adapted in a straightforward manner for a non-Newtonian fluid. First, the integral momentum flux upstream of the nozzle exit, see Eq. (4b), will be different, since the assumption of Poiseuille flow breaks down. Second, the integral of the axial deviatoric stress over the nozzle exit plane will be nonzero in the integral balances for the nozzle and the jet region, Eqs. (6) and (10), respectively. In the overall momentum balance, Eq. (14), this term is still absent as the contributions from the nozzle and the jet region cancel each other. Third, the same decomposition as for the viscous force of Newtonian fluid can be made for the viscoelastic force of a non-Newtonian fluid; see Eqs. (16a)–(16c). However, the expressions for the excess wall pressure drop and the excess integral wall shear stress need to be modified, as the reference state is different from homogeneous Poiseuille flow.

In our analysis, we assumed the presence of Poiseuille flow with a parabolic velocity profile at some distance upstream of the nozzle exit. This is justified only when Re $\lesssim 2000$, as otherwise the flow may not be laminar anymore, and when the nozzle is sufficiently long such that Poiseuille flow can develop within the nozzle. If these conditions are not satisfied, then the integral momentum balance needs to be modified along the lines just discussed for a non-Newtonian fluid, except that the integral of the axial deviatoric (viscous) stress over the nozzle exit plane is still zero. For a laminar flow, Gavis and Modan [7] performed experiments to assess the effect of nozzle length on the jet contraction ratio. For Re > 16, they observed that the jet contraction ratio was larger for a smaller nozzle length/diameter ratio. Furthermore, the contraction ratio went through a minimum in the Reynolds number and then increased again with Re. This was attributed to a lack of flow development within the nozzle, resulting in a reduced integral momentum flux at the nozzle exit with respect to the value expected for Poiseuille flow; see Eq. (4b). Our analysis supports their interpretation: in the inertial flow regime (Re $\gg 1$ and We $\gg 1$), the factor 4/3 on the left-hand side of Eq. (15) will be smaller and closer to one when the flow is not fully developed and it will depend on $L/(R \cdot \mathrm{Re})$ with L the nozzle length, assuming that the flow development length scales linearly with $R \cdot \mathrm{Re}$. Hence, χ will be higher than Harmon's limit of $\sqrt{3}/2$ in this case.

The assumption of Poiseuille flow may even completely break down when the nozzle length becomes on the order of the nozzle diameter. For example, for a liquid jet issued from a large vessel through a Borda's mouthpiece, the flow within the nozzle may be close to irrotational, resulting in a jet contraction ratio of $\chi = \sqrt{2}/2 \approx 0.71$ [36], which is significantly below Harmon's limit for Poiseuille flow. This result is expected to hold when Re is high (negligible frictional pressure drop over the nozzle), We is high (negligible surface tension) and the nozzle has a finite length and projects into the vessel (stagnant flow near the vessel walls) [37]. This example illustrates that an accurate prediction of the jet contraction ratio in practical applications requires detailed knowledge of both the nozzle geometry and the flow conditions at the nozzle inlet (for instance, in case of a Borda's mouthpiece, the velocity field is not unidirectional and the pressure profile is not uniform at the inlet of the nozzle).

Thin liquid jets are prone to a capillary instability driven by surface tension, resulting in the formation of liquid drops [30]. In applications such as prilling [38], this instability is utilized, for example, to produce fertilizer granules from molten urea. In studies of jet breakup, it is often implicitly assumed that the flow within the undisturbed jet is uniform and that the jet radius is constant and equal to the radius of the nozzle from which the jet is issued. The present work shows that the upstream flow conditions and nozzle geometry matter. For a long nozzle with a parabolic velocity profile at some distance upstream of the nozzle exit, the jet significantly contracts at the Reynolds numbers typical for prilling applications. Since a jet breaks up at a length scale proportional to the undisturbed jet radius, this thus has consequences for the optimal perturbation frequency for jet breakup and the resultant droplet and granule size distributions. This was already analyzed by Harmon [5] for the high-Re limit (inertial regime) using results from linear temporal stability analysis, but his analysis can be extended to lower Reynolds numbers using Joseph's correlation, Eq. (25). Assuming a harmonic perturbation of the jet at the optimal frequency for breakup, the diameter, d_s, of the spherical granules is expected to be

$$\frac{d_s}{R} = \frac{1.63(1 + 3\,\mathrm{Oh}/\sqrt{2})^{1/6}}{\sqrt{1 - 1.48\,\mathrm{Re}^{-2/3}}} \quad (\mathrm{Ca} \gg 1, \mathrm{Re} \gtrsim 10), \tag{35a}$$

where the Ohnsesorge number, $\mathrm{Oh} = \sqrt{2\,\mathrm{Ca}/\mathrm{Re}}$, accounts for the influence of the liquid viscosity on the breakup process. Harmon's result for the expected granule size corresponds to the limit of $\mathrm{Re} \to \infty$.

The contraction of the jet also affects the optimal perturbation frequency. Given that $f_{\mathrm{opt}} = U_\infty/\lambda_{\mathrm{opt}}$, the following expression can be derived for the optimal perturbation frequency:

$$\frac{f_{\mathrm{opt}}\,R}{U_b} = \frac{7.31 \times 10^{-2}}{(1 + 3\,\mathrm{Oh}/\sqrt{2})^{1/2}(1 - 1.48\mathrm{Re}^{-2/3})^{3/2}} \quad (\mathrm{Ca} \gg 1, \mathrm{Re} \gtrsim 10). \tag{35b}$$

For $\mathrm{Re} > 14.4$, the contraction of the jet is responsible for an increase in the optimal perturbation frequency. For $\mathrm{Re} \to \infty$, the frequency is even a factor of 1.54 higher, which underlines the significant effect of the jet contraction behavior near the nozzle on the breakup of the jet further downstream.

In the above discussion, we implicitly assumed that the jet contraction does not influence the jet stability other than through a change of the equilibrium jet diameter and velocity with respect to the conditions at the nozzle exit. However, the jet contraction and relaxation of the velocity profile do matter when the jet is subjected to an imposed perturbation at the nozzle exit. This was analyzed by Sevilla [31] for $\mathrm{Re} \gg 1$ and assuming a parabolic velocity profile at the nozzle exit. First, the unperturbed jet velocity field was obtained from numerically solving the axisymmetric boundary-layer equations. Next, a linear spatiotemporal stability analysis was conducted using a quasi-parallel approach to study the local jet stability as a function of the streamwise distance from the nozzle exit. The flow was found to be convectively unstable throughout the jet down to a critical Weber number, $\mathrm{We}_c(\mathrm{Re})$, below which a local region emerged near the nozzle in which the flow was absolutely unstable, marking the transition from a jetting to a dripping regime. Interestingly, the $\mathrm{We}_c(\mathrm{Re})$-curve was strongly different from the corresponding curve for a cylindrical jet with a uniform velocity profile [39]. Although the assumption of a parabolic velocity profile breaks down for the lower Re range studied by Sevilla [31], this study underlines the important effect of the jet relaxation region on the jet stability.

ACKNOWLEDGMENT

This work was executed as part of the Ph.D. research of the second author. We acknowledge the financial support of Machinefabriek Kreber BV under a TU Delft/Kreber Research Agreement.

DATA AVAILABILITY

The data underlying the figures and the OpenFoam case files for a selected case are publicly available in the 4TU.ResearchData repository [40].

---

[1] A. C. Merrington, Flow of visco-elastic materials in capillaries, Nature (London) **152**, 663 (1943).
[2] J.-Z. Liang, Predictions of normal stress difference during circular duct flow of polymer melts, Polym. Test. **21**, 619 (2002).
[3] R. I. Tanner, A theory of die-swell revisited, J. Non-Newtonian Fluid Mech. **129**, 85 (2005).
[4] S. Middleman and J. Gavis, Expansion and contraction of capillary jets of Newtonian liquids, Phys. Fluids **4**, 355 (1961).
[5] D. B. Harmon, Drop sizes from low speed jets, J. Franklin Inst. **259**, 519 (1955).
[6] J. Batchelor, J. P. Berry, and F. Horsfall, Die swell in elastic and viscous fluids, Polymer **14**, 297 (1973).
[7] J. Gavis and M. Modan, Expansion and contraction of jets of Newtonian liquids in air: Effect of tube length, Phys. Fluids **10**, 487 (1967).
[8] R. E. Nickell, R. I. Tanner, and B. Caswell, The solution of viscous incompressible jet and free-surface flows using finite-element methods, J. Fluid Mech. **65**, 189 (1974).
[9] H. D. Haustein, R. S. Harnik, and W. Rohlfs, A simple hydrodynamic model of a laminar free-surface jet in horizontal or vertical flight, Phys. Fluids **29**, 082105 (2017).
[10] S. L. Goren and S. Wronski, The shape of low-speed capillary jets of Newtonian liquids, J. Fluid Mech. **25**, 185 (1966).
[11] R. Gear, M. Keentok, J. Milthorpe, and R. Tanner, The shape of low Reynolds number jets, Phys. Fluids **26**, 7 (1983).
[12] N. Bohr, Determination of the surface-tension of water by the method of jet vibration, Philos. Trans. R. Soc. A **209**, 281 (1909).
[13] S. L. Goren, Development of the boundary layer at a free surface from a uniform shear flow, J. Fluid Mech. **25**, 87 (1966).
[14] J. P. K. Tillett, On the laminar flow in a free jet of liquid at high Reynolds numbers, J. Fluid Mech. **32**, 273 (1968).
[15] J. L. Duda and J. S. Vrentas, Fluid mechanics of laminar liquid jets, Chem. Eng. Sci. **22**, 855 (1967).
[16] C. Philippe and P. Dumargue, Étude de l'établissement d'un jet liquide laminaire émergeant d'une conduite cylindrique verticale semi-infinie et soumis à l'influence de la gravité, Z. Angew. Math. Phys. **42**, 227 (1991).
[17] C. Philippe and C. Froehly, Mesures de vitesses dans un écoulement laminaire axisymétrique par une technique optique de visualisation en lumière cohérente, Z. angew. Math. Phys. **34**, 137 (1983).
[18] S. A. Trogdon and D. D. Joseph, The stick-slip problem for a round jet: I. Large surface tension, Rheol. Acta **19**, 404 (1980).

[19] S. A. Trogdon and D. D. Joseph, The stick-slip problem for a round jet: II. Small surface tension, Rheol. Acta **20**, 1 (1981).
[20] E. Mitsoulis, G. C. Georgiou, and Z. Kountouriotis, A study of various factors affecting Newtonian extrudate swell, Comput. Fluids **57**, 195 (2012).
[21] G. C. Georgiou and A. G. Boudouvis, Converged solutions of the Newtonian extrudate-swell problem, Int. J. Numer. Methods Fluids **29**, 363 (1999).
[22] D. D. Joseph, Slow motion and viscometric motion: Stability and bifurcation of the rest state of a simple fluid, Arch. Ration. Mech. Anal. **56**, 99 (1974).
[23] B. J. Omodei, On the die-swell of an axisymmetric Newtonian jet, Comput. Fluids **8**, 275 (1980).
[24] G. C. Georgiou, T. C. Papanastasiou, and J. O. Wilkes, Laminar Newtonian jets at high Reynolds number and high surface tension, AIChE J. **34**, 1559 (1988).
[25] H. Jasak, A. Jemcov, and Z. Tukovic, OpenFOAM: A C + + library for complex physics simulations, in *Proceedings of the International Workshop on Coupled Methods in Numerical Dynamics* (Dubrovnik, Croatia, 2007), pp. 1–20.
[26] J. Gavis, Contribution of surface tension to expansion and contraction of capillary jets, Phys. Fluids **7**, 1097 (1964).
[27] S. Middleman, *Modeling Axisymmetric Flows: Dynamics of Films, Jets, and Drops* (Academic Press, San Diego, CA, 1995).
[28] J. C. Slattery and W. R. Schowalter, Effect of surface tension in the measurement of the average normal stress at the exit of a capillary tube through an analysis of the capillary jet, J. Appl. Polym. Sci. **8**, 1941 (1964).
[29] S. Richardson, A 'stick-slip' problem related to the motion of a free jet at low Reynolds numbers, in *Mathematical Proceedings of the Cambridge Philosophical Society*, Vol. 67 (Cambridge University Press, Cambridge, UK, 1970), p. 477.
[30] J. Eggers and E. Villermaux, Physics of liquid jets, Rep. Prog. Phys. **71**, 036601 (2008).
[31] A. Sevilla, The effect of viscous relaxation on the spatiotemporal stability of capillary jets, J. Fluid. Mech. **684**, 204 (2011).
[32] F. Pimenta and M. A. Alves, Stabilization of an open-source finite-volume solver for viscoelastic fluid flows, J. Non-Newtonian Fluid Mech. **239**, 85 (2017).
[33] R. Comminal, F. Pimenta, J. H. Hattel, M. A. Alves, and J. Spangenberg, Numerical simulation of the planar extrudate swell of pseudoplastic and viscoelastic fluids with the streamfunction and the VOF methods, J. Non-Newtonian Fluid Mech. **252**, 1 (2018).
[34] S. S. Deshpande, L. Anumolu, and M. F. Trujillo, Evaluating the performance of the two-phase flow solver interFoam, Comput. Sci. Discov. **5**, 014016 (2013).
[35] J. S. Vrentas and C. M. Vrentas, Inertia and surface tension effects in Newtonian liquid jets, Int. J. Multiphase Flow **8**, 559 (1982).
[36] G. K. Batchelor, *An Introduction to Fluid Dynamics* (Cambridge University Press, Cambridge, UK, 2000).
[37] W.-G. Dong and J. H. Lienhard, Contraction coefficients for Borda mouthpieces, J. Fluids Eng. **108**, 377 (1986).
[38] Y. E. Kamis, S. Prakash, W.-P. Breugem, and H. B. Eral, Controlling the breakup of spiralling jets: Results from experiments, nonlinear simulations and linear stability analysis, J. Fluid Mech. **956**, A24 (2023).
[39] S. J. Leib and M. E. Goldstein, Convective and absolute instability of a viscous liquid jet, Phys. Fluids **29**, 952 (1986).
[40] https://doi.org/10.4121/4db38f99-8733-402c-bf12-a4f285fb5759